Degradation of Mechanical Properties of U-Mo Alloy from the Un-irradiated to Irradiated State

A Thesis
Presented in Partial Fulfillment of the Requirements for the
Degree of Master of Science
with a
Major in Mechanical Engineering
College of Graduate Studies
University of Idaho
by

Jason L. Schulthess

Major Professor: Richard Christensen, Ph.D.
Committee Members: Jim Cole, Ph.D.; Indrajit Charit, Ph.D.
Department Administrator: Steven Beyerlein, Ph.D

December 2018

Authorization to Submit Thesis

This thesis of Jason L. Schulthess, submitted for the degree of Master of Science with a Major in Mechanical Engineering and titled “Degradation of Mechanical Properties of U-Mo Alloy from the Un-irradiated to Irradiated State,” has been reviewed in final form. Permission, as indicated by the signatures and dates below, is now granted to submit final copies to the College of Graduate Studies for approval.

Major Professor: _____ Date: _____
Richard Christensen, Ph.D

Committee Members: _____ Date: _____
Jim Cole, Ph.D.

_____ Date: _____
Indrajit Charit, Ph.D.

Department
Administrator: _____ Date: _____
Steven Beyerlein, Ph.D

Abstract

Studies were conducted to establish the mechanical properties of uranium-10 wt.% molybdenum (U–10Mo) in both the un-irradiated condition and after neutron irradiation. In the un-irradiated condition, mechanical properties were obtained for various temperatures and after the alloy had been wrought processed by rolling into four different rolling conditions. The irradiated mechanical properties were obtained at various fission densities and then the degradation of the mechanical properties from the un-irradiated to irradiated condition evaluated and a correlation with porosity developed. The mechanical properties obtained of the un-irradiated material differed from that previously published in the literature, which was expected due to the differences in thermomechanical processing conditions between the materials evaluated. The mechanical properties degraded as fission density increased as expected, and correlate to the increase of porosity that develops with increasing fission density.

Acknowledgements

Acknowledgement is given to the various personnel at Idaho National Laboratory (INL) and the University of Idaho for guiding me through this process, and who's mentoring, and curiosity helped shape this work. Particular thanks go to Dr. Barry Rabin and Dr. Jim Cole for helping to bring the conceptual idea to reality and providing the funding for accomplishing the work. To Mr. Randy Lloyd and Dr. Thomas Walters for their assistance and guidance on setting up the experiments and analyzing the data. To Mr. Michael Heighes and Ms. Katelyn Wheeler for their assistance in executing the experimental work. To Dr. Tammy Trowbridge, and Dr. Emmanuel Perez for their assistance in preparing samples for microscopy and obtaining microscopy images, and consulting on the results. Finally to Mr. Glenn Moore and Mr. Mike Chapple for fabricating the source material for the work. Many others, especially at the Fuels and Applied Science Building (FASB) and the Hot Fuel Examination Facility (HFEF) facility at INL including facility managers, shift supervisors, technicians, and radiological controls personnel who enabled the work to be accomplished.

Additional thanks and acknowledgement go to Dr. Richard Christensen and Ms. Alice Allen of University of Idaho for helping me to reach the finish line when the finish line appeared to be so far away.

Table of Contents

List of Figures

List of Tables

1 CHAPTER 1: INTRODUCTION

High density low enriched uranium molybdenum (U-Mo) alloy fuels in a monolithic foil form (see Figure 3.1) are being developed to support conversion of high performance research and test reactors from a fuel that requires high enrichment (greater than 20 wt% U-235) to a low enriched fuel (less than 20 wt% U-235). In order to achieve the high densities required to support reactor conversion, the fuel is fabricated using thermomechanical wrought processing by rolling. More specifically, following casting of the appropriate alloy, the fuel system foil is fabricated by sequential process of hot co-rolling (~650 °C) followed by thickness reductions by cold rolling. The foil is then clad in aluminum by hot-isostatic pressing (at ~520 to 580°C), as illustrated in Figure 3.1The specific thermomechanical processing history being proposed for this fuel form, and evaluated in this work is different from any thermomechanical processing history for U-Mo alloy that is in the existing literature. The specific thermomechanical processing history, and review of existing data in the literature is discussed in more detail in later chapters. This results in a knowledge gap of the exact mechanical properties of the proposed U-Mo alloy. Knowledge of the actual mechanical properties of the as fabricated fuel is a requirement to support fuel performance evaluations, and eventual qualification of the fuel for deployment.

Part 1 of this thesis, contained in chapter two, obtains the mechanical properties of un-irradiated U-10Mo alloy. Specifically, this work aimed to evaluate differences in mechanical properties that would result from variations in the thermomechanical wrought rolling step during fabrication. These results inform modeling efforts, fabrication process development, and ultimately support qualification of the fuel for reactor conversion.

Fresh, un-irradiated, or starting properties, however, is only part of the story with respect to demonstrating the mechanical integrity of the fuel and fuel performance during irradiation. For this, it is necessary to obtain mechanical properties of the fuel at various end states with respect to irradiation or fission density of the fuel. As with the un-irradiated mechanical properties, no data was found in the literature that was representative of the irradiation conditions that are proposed for this fuel form. A review of the existing literature is contained in later chapters.

Part 2 of this thesis, contained in chapter three, obtains the mechanical properties of irradiated U-10Mo alloy. Specifically evaluated are the properties at different fission densities to identify the degradation of mechanical properties as the fission density (or fuel burnup) increases. It is proposed and evaluated in this chapter that the degradation of mechanical properties with increasing fission density is likely directly attributable to the increase of porosity that accompanies irradiation. Several existing porosity/mechanical properties correlations are evaluated to examine representativeness to the data obtained in this work.

The choice to format this thesis into these two parts is concomitant with the separation of these two parts for publication. Part 1, as previously described, and contained in chapter 2 has been accepted for publication as written. Part 2, as previously described, and contained in chapter 3 has been submitted for publication and is currently under review.

Relevant literature review, methodologies, results, discussion of results and uncertainties, and conclusions are therefore contained in each chapter.

2 CHAPTER 2: ELEVATED TEMPERATURE TENSILE TESTS ON DU-10MO ROLLED FOILS

"Elevated Temperature Tensile Tests on DU-10Mo Rolled Foils." *Journal of Nuclear Materials,* 510 (2018) 282-296

2.1 Abstract

Studies were completed to obtain tensile mechanical properties for uranium-10 wt.% molybdenum (U–10Mo) foils which were subjected to four different thermomechanical processing conditions. U-Mo alloy foils are being investigated to support fuel conversion of high power research reactors from their current high enriched fuel form to a low enriched fuel form. Mechanical properties of the fuel foil have an effect on irradiation performance and fuel fabrication and therefore are required to support modeling and qualification of new low-enriched uranium monolithic fuel plate designs. The data contained in this document contributes to fuel qualification by fulfilling the requirement that physical properties related to fuel meat be established. It is expected that depleted uranium-10 wt% Mo (DU–10Mo) mechanical behavior is representative of the low-enriched U–10Mo to be used in actual fuel plates; therefore DU–10Mo was studied to simplify material processing, handling, and testing requirements. In this report, the different thermomechanical treatments included variations of wrought hot and cold rolling reduction and post rolling annealing. Each of the four foils was hot rolled. After hot rolling reduction, three of the four foils were further reduced by cold rolling. One of the three was reduced a further 20% by cold rolling, and the remaining two were reduced 50% by cold rolling. Following cold rolling reduction, one of the two foils which had been reduced 50% by cold rolling was annealed at 650°C. Performing this analysis allows assessment of the impact of foil fabrication history on the resultant tensile properties DU–10Mo fuel foils.

Tensile properties of DU–10Mo at room temperature through approximately 400°C determined from the tests conducted herein suggest the material is stronger and has lower ductility than what has been reported previously in the literature. The explanation for these differences has yet to be determined, but is likely related to differences in grain size and/or impurity content, and variation in fabrication history. At the highest temperatures tested (550°C) better agreement between the values reported here and available literature was found. As expected, yield and ultimate tensile strength decreased with increasing test temperature. Generally, the yield stress for all foil processing conditions was found to be in the range of 1100 MPa for room temperature tests, and in the range of 200 MPa for tests

conducted at 550°C. Ultimate tensile stress was in the range of 1175 MPa at room temperature, decreasing to approximately 225 MPa at 550°C. Elongation increased significantly, from 0–2% at room temperature to 50% or more for the tests at 550°C.

2.2 **Introduction**

High density low enriched uranium molybdenum (U-Mo) alloy fuels in a monolithic foil form are being developed to support conversion of high performance research and test reactors from a high enriched fuel (greater than 20 wt% U-235) to a low enriched fuel (less than 20 wt% U-235) [1]. Mechanical properties of the fuel foil have an effect on irradiation performance and fuel fabrication processes and are required to support fuel performance modeling and regulatory qualification of new low-enriched uranium monolithic fuel plate designs [2]. For example, Hu et al, (2015) used grain size, grain morphology, and fission gas bubble size and morphology to numerically model and predict impact on thermal conductivity of U-Mo alloys [3]. Similarly, Wang et al used existing experimental data combined with thermodynamic models to develop phase diagrams and thermodynamic properties in the Al-U and Co-U binary systems [4].

During irradiation, the fuel is required to maintain mechanical integrity. To establish this, it is necessary to understand the mechanical response of the fuel meat such that irradiation-induced changes to fuel properties do not lead to loss of fuel-system mechanical integrity. Fabrication history and thermal treatment of the U-Mo alloy has an impact on resultant mechanical properties, which was shown by Waldron (1958) by comparing the properties of U-10.9Mo in the as-cast/heat treated versus extruded condition and found that the extruded material was both stronger and more ductile than the cast material [5]. Therefore, this study aims to establish the pre irradiation mechanical tensile properties for rolled uranimum–10 wt.% molybdenum (U–10Mo) foils that have been subjected to four different thermomechanical wrought rolling conditions. The mechanical properties of the foil as a result of rolling is of specific interest as wrought processing by rolling is generally how foils are fabricated for this fuel type. A description of the general fuel fabrication process, including the process used for this material is included in the materials section.

Mechanical properties data is frequently used to support fabrication development. Soulami et al, (2017) [6], used existing data in the literature to numerically model roll-separation force

and effects during rolling of U-10Mo alloys. Likewise, fuel performance models that evaluate in-pile thermomechanical behavior also make use of this fundamental mechanical properties data. Ozaltun et al, in several papers report the use of existing experimental U-10Mo mechanical properties data to predict fuel performance issues related to mechanical integrity such as residual stress and thermal cycling [7, 8, 9, 10, 11, 12, 13].

Limited data exist on the property-processing-structure relationship of U–10Mo fuel foils. Most of the available studies reporting properties for U-Mo alloys were conducted in the 1950s and 1960s. For example, Waldron (1958) reports yield stress, ultimate tensile stress, and modulus for U-Mo alloys, where the wt% of Mo was varied in the alloy and where the heat treatment temperature and time were varied [5]. However, the Waldron report does not provide information relevant to the properties of rolled foils, or the effect of foil rolling conditions on properties.

Likewise, Kalashnikov et al. (1959) [14] reported mechanical properties for U-Mo alloys produced by hot rolling at temperatures between 900-1200°C, followed by water-quenching from 900°C. Specimens were held at 900°C for 7 days. Kalashnikov et al. varied the Mo content of the alloys tested. As before, in Waldron (1958) [5], Kalashnikov et al (1959) [14] do not provide mechanical properties for cold rolling, nor do the specific hot-rolling conditions match the work reported here as the hot rolling of the present work was performed at 650°C.

Others, such as Joshi et al. [15] and [16], evaluated the mechanical properties of as-cast or homogenized U–10Mo alloy in the form of pins via compression testing at various temperatures. The as-cast or homogenized condition noted by Joshi et al. documents the initial and intermediate microstructure and mechanical properties in the thermomechanical processing history of the foils evaluated in this work.

Other previous work by various authors to establish tensile mechanical properties of U–10Mo alloy is summarized by Ozaltun et al. in [7] and includes the work by Burkes et al (2010) [17] who hot rolled the material, and that of Mihalczo (1962) [18] who used cast and machined material. The work of Waldron (1958) [5], Kalashnikov (1959) [14] and the authors summarized by Ozaltun [7] is summarized here for convenience and is presented in Table 2.1. Burkes et al (2009) [19] also summarized previous work reporting mechanical properties of U-Mo alloys. These results include variations of hardness as a function of temperature or are reported based on variation of Mo content in the alloy [5, 20, 21, 22, 23,

24, 25]. Yield stress, ultimate tensile stress, and elongation all increase with increasing Mo content and is attributed to the improved resistance to bulk plastic deformation through increased addition of Mo and associated hardening effect in the γ phase. Burkes et all (2009) compare their results to previous available literature, but note that differences in homogenization treatment, specimen geometry and strain rates makes direct comparison difficult [25].

Because of the importance of basic strength and modulus data for fabrication development and fuel performance modeling, an expanded set of mechanical properties for various foil-rolling conditions typical of fuel-foil manufacturing is necessary. This work aims to evaluate the mechanical properties of U–10Mo alloys under various representative rolling conditions to inform modeling efforts, fabrication process development, and ultimately, to support fuel qualification and reactor conversion.

Table 2.1. Summarized U-10Mo alloy mechanical properties from literature

Reference Source	Form Tested	Prior Heat Treatment Temp (°C)	Prior Heat Treatment Time (Days)	Temp of Testing (°C)	Yield Stress (MPa)[a]	UTS (MPa)[a, b]	Youngs Modulus (GPa)[a]	Elongation (%)	Carbon Content (ppm)
Waldron	As-cast	900	7	20	NA	617.8	86.87	0.1	~700
Waldron	As-cast	450	14	20	NA	293.7	119.3	0.8	~700
Ozaltun	Hot Rolled with 90% reduction at 650 °C; annealed at either 650 °C or 675 °C for durations of 0.5, 1 or 2 h	NA	NA	21	780	790	65	NA	~54-410
Ozaltun	Cast and machined	NA	NA	94	760	760	NA	NA	NA
Waldron	As-cast	900	7	200	NA	510.2	73.77	0.5	~700
Waldron	As-cast	450	14	200	NA	303.4	91.7	Nil	~700
Kalashnikov	Hot Rolled between 900-	NA	NA	200	NA	578.6	NA	0.5	NA

	1200°C followed by water quenching from 900°C. Held at 900°C for 7 days								
Ozaltun	Cast and machined	NA	NA	205	655	655	NA	NA	NA
Waldron	As-cast	450	14	300	NA	183.4	103.4	0.5	~700
Ozaltun	Cast and machined	NA	NA	316	527	536	NA	NA	NA
Waldron	As-cast	900	7	400	NA	358.5	51.71	1	~700
Waldron	As-cast	450	14	400	NA	256.5	108.9	0.5	~700
Waldron	As-cast	575	28	400	NA	148.9	84.12	2	~700
	Hot Rolled between 900-1200°C followed by water quenching from 900°C. Held at 900°C for 7 days								
Kalashnikov		NA	NA	400	NA	397.2	NA	1	NA
Ozaltun	Cast and machined	NA	NA	427	474	511	NA	NA	NA

Ozaltun	Cast and machined	NA	NA	538	427	440	NA	NA	NA
Waldron	As-cast	900	7	600	NA	179.3	33.09	0	~700
Waldron	As-cast	575	28	600	NA	124.1	59.29	0.5	~700
Kalashnikov	Hot Rolled between 900-1200°C followed by water quenching from 900°C. Held at 900°C for 7 days	NA	NA	600	NA	194.2	NA	NA	NA
Waldron	As-cast	900	7	800	NA	55.16	41.37	3	~700
Waldron	As-cast	575	28	800	NA	86.9	59.29	11	~700
Kalashnikov	Hot Rolled between 900-1200°C followed by water quenching from 900°C. Held at 900°C for 7 days	NA	NA	800	NA	62.8	NA	30	NA

a. These values are calculated conversion from the published data for the purpose of comparison.

b. Kalashnikov does not specifically identify these values as ultimate tensile strength (UTS), but context of the paper infers these values as UTS values.

c. Where value is noted as NA, information was not provided in the source reference.

2.3 Experimental Procedure

2.3.1 Materials

The general fabrication process of the U-Mo monolithic fuel is 1) alloying and casting, 2) foil rolling, 3) bonding of the cladding, and 4) finishing and inspection for quality assurance. The fabrication process is continually being refined and the following paragraphs provide additional details of the process at the time the material in this study was fabricated.

A depleted uranium (DU) with 10 weight% molybdenum (DU-10Mo) log was vacuum induction cast in the Y-12 development facility into a coated graphite mold. The log casting was then broken into chunks and recast into a graphite plate mold. A coupon was machined from the plate, designated #551, and shipped to INL. It is noted that from the time the source material was produced at Y-12 to now, the casting process has evolved. Consideration should be taken if material properties are compared from this work to material produced using the more recently evolved casting process. All tests contained in this document were performed using this source material. Chemistry data for the source material is included in Table 2.2. Of note is that the carbon content of the source material is ~710 ppm. This value of carbon content is similar to the material used by Waldron [5] but is greater, by several hundred ppm, than that used by Burkes [17].

The coupon was sectioned into four pieces by INL using wire electric discharge machining (wire EDM), and each piece was homogenized at 1000°C for two hours under vacuum of 5×10^{-6} Torr. These pieces were then placed into hermetically sealed cans to prevent oxidation while heating and performing the hot rolling operation. The pieces where then individually hot-rolled after preheating the can at 650°C for ~30 minutes. Cans were passed through a Fenn two-high rolling mill several times, with an initial reduction of 10% and decreased to 5% as the process continued resulting in a bare foil extracted from the process. The foil thickness after hot rolling varied with each foil condition as the thickness was an input to the intended follow on cold rolling step. The number of passes for each foil varied based on the target reductions planned for cold rolling. As needed, the can was placed back into the box furnace and reheated to 650°C and allowed to soak for between 5 and 15 minutes in order to maintain the target rolling temperature of 650°C. The thickness of the foil after hot rolling for each of the four conditions is contained in the following paragraph. The thickness however was not directly measured and instead is taken from the target thickness in the rolling schedule except for in the hot-rolled only case where the thickness was directly measured.

During normal fabrication of the fuel, a layer of zirconium would be included during the hot rolling process to roll-bond the zirconium to the U-Mo foil. However, for this specific investigation, no zirconium was included as it was desired to test the properties of the bare foil rather than a composite material.

After hot rolling, the foil is removed from the can and cold rolled directly on the same Fenn two-high rolling mill. Additional cold rolling was performed on three of the four foils to bring the final thickness of each cold-rolled foil to a target of 0.38 mm, representative of the final thickness of actual fuel foils. The four foil conditions studied are described in the following list. A short hand description of each condition is also included in the following list, and is used throughout this document. Additional information on processing of the monolithic foils can be found in Clark et al (2003 and 2006) [26, 27].

1. Foil 551-2, hot rolled from ~3.66 mm to ~0.762 mm (79% reduction), followed by additional 50% cold-rolling reduction to ~0.38 mm; 551-2 50%CW
2. Foil 551-3, hot rolled from ~3.66 mm to ~0.762 mm (79% reduction), followed by additional 50% cold-rolling reduction to ~0.38 mm, followed by stress-relief annealing at 650°C for one hour; 551-3 50% CW+A
3. Foil 551-4, hot rolled from ~3.66 mm to ~0.483 mm (87% reduction), followed by additional 20% cold-rolling reduction to ~0.38 mm; 551-4 20% CW
4. Foil 551-5, hot rolled from ~3.66 mm to ~0.540 mm (85% reduction) no further processing, i.e. hot-rolled only; 551-5 HR Only

In the general fuel fabrication process, the resultant foils are then placed between two layers of aluminum (Al), and then placed in another encapsulated can for hot isostatic press (HIP) processing to bond the Al to the fuel foil. The HIP process is typically conducted at a temperature of 560°C for a time of 90 minutes. Post HIP, the can is opened, the bonded plates removed, and the plates are finished to final dimensions and inspected. [28, 29]. The HIP process was not performed on this material as the investigation was focused on the properties of the bare foil and not the composite fuel plate.

Table 2.2. Chemistry report provided by Y–12 for log 3C32-WP-TRN0. Impurity levels over 25 ppm reported. Impurity values less than 25 ppm where provided in the chemistry report from Y–12 but are not reported here.

3C32-WP-TRNO	%Mo	ppm C	ppm Al	ppm Cu	ppm Er	ppm Fe	ppm K	ppm Mn	Ppm Ni	ppm P	ppm Si	ppm W
Top	10.40	706	60	13	5.9	160	32	28	37	<20	250	28
Middle	10.50	714	60	13	28	160	<16	29	39	<20	250	25
Bottom	10.30	722	61	12	3.0	160	21	29	38	<20	240	25

2.3.2 Sample Preparation

These simulated fuel foils were fabricated using a depleted uranium (DU) - molybdenum alloy to simulate actual fuel foils made with low-enriched uranium (LEU). Flat, rectangular tensile specimens were cut from the foils. The size of the flat rectangular specimens corresponds to a reduced sub-size specimen, as described in Figure 1 of ASTM E8/8M-13 [31], with an additional size reduction of 50%, as shown in [30]. The specimens were cut from the foil sheet using wire EDM machining. Specimens were sectioned from the sheet with the tensile axis both parallel and transverse to the foil-rolling direction to assess potential effects of rolling texture on mechanical properties. The resultant specimens have a nominal overall length of 50.8 mm, a reduced section width of 3.2 mm, and a reduced section length of 16 mm. The small specimen size is necessary due to size limitations imposed by the furnace internal dimensions and material availability.

Tests were conducted on specimens with both longitudinal and transverse orientation relative to rolling direction, and at various temperatures between room temperature (per ASTM E8/8M-13) and elevated temperatures (per ASTM E21-10) up to 550°C.

2.3.3 Testing Procedure

The testing system incorporates a standard Instron 3366 table-top test machine, Instron 5 kN load cell, Instron high-temperature wedge grips, and a C-M 1608-series environmental furnace. Tests were controlled and data collected by Instron Bluehill version 3.41 software. The system was developed, calibrated, and verified for performing this series of tests. The system includes an environmental-control furnace that allows elevated-temperature tensile testing in an inert-argon-gas environment with low oxygen concentration, preventing rapid oxidation or oxygen embrittlement of the DU–10Mo test specimens. Argon gas flowed through the furnace at a flow rate of ~424 L/min. O_2 concentration levels were measured with a Delta-F Oxygen Analyzer (DF-130ε) at a rate of 1.5 L/min. During elevated temperature testing, typical O_2 concentration values were less than 5 ppm. Using this test set up, for a nominal specimen cross-section of 1.2 mm², the maximum potential stress error is ±10 MPa. Additional details for the experimental set up are found in [30].

Room-temperature testing was completed using a small 12.7 mm gauge-length extensometer from Epsilon Corp. The extensometer has a measuring range to +20% tensile strain.

The test system and environmental-control furnace used for elevated-temperature testing precluded use of specimen-mounted extensometry for strain measurement. In lieu of direct strain measurement, the test system compliance was measured at room temperature, and a quadratic strain-estimating function was developed. Additional details can be found in [30].

ASTM E8/8M-13 [31] or ASTM E21-10 [32] guided room and elevated-temperature testing, respectively. Room-temperature tests occurred in an air environment and helped establish baseline properties for each material condition. Elevated-temperature tests were performed at the following temperatures: 200, 250, 350, 400, 450, 550°C in an argon-gas environment. Elevated-temperature tests were conducted with the test temperature within ±5°C of the target temperature. Specimens were subjected to elevated temperature for only the time it took for the furnace to heat up the specimen to the desired target temperature, and the time to perform the test. Tests were initiated immediately once the specimen reached the desired target temperature. Heat up times for all of the test temperatures was ~2-3 hours. Testing time increased with increasing temperature due to increased specimen ductility and ranged from ~5 minutes at 200°C to ~20 minutes at 550°C.

Room- and elevated-temperature tests were run at a constant crosshead speed of 0.2 mm/min, producing a nominal specimen strain rate of 0.5%/min. This rate meets the requirements of both ASTM E8-13 (for room-temperature [31] and E21-10 (for elevated-temperature [32]) tensile-testing standards.

For all tests, the 0.2% offset method was used to determine yield strength. Elongation was determined after fracture occurred based on the gauge length of ~12.7 mm. Calculated values were rounded up or down to the nearest digit of the required accuracy (standard rounding method), excepting that in accordance with the test standard, final specimen elongation values were rounded to the nearest 0.2% deformation interval.

In multiple cases, test results for an individual specimen were invalidated by specimen failure outside of the allowable region or, infrequently, due to other problems with a particular specimen. Replicate specimens under replicate test conditions were tested to obtain the required number of valid tests for that particular material/test condition combination.

Tests that did not fail in the middle 50% of gauge length were considered invalid and not included in results. Some specimens failed prior to the stress-strain curve intersecting the

0.2% offset curve; these specimens do not provide a valid yield-strength value and thus are not included in the reporting of yield strength

2.3.4 Specimen Characterization and Metallography

Metallography of selected specimens was performed to investigate the base nature of the material in order to elucidate contributing features to the noted failure mechanisms. A JEOL JSM 6610LV Scanning Electron Microscope (SEM) equipped with secondary electron and backscatter detectors, Energy Dispersive Spectroscopy (EDS), and Electron Backscatter diffraction (EBSD), was used to produce micrographs of the longitudinal and transverse cross-section from the samples. The EDAX™ Orientation Imaging Microscopy™ (OIM™) version 7.3 was used to collect and analyze the EBSD data. The longitudinal and transverse directions of this work reference to the rolling direction.

Grain microstructure and sizes were determined in each of the as-fabricated rolling conditions by EBSD in the SEM. Because U-Mo alloys are prone to rapid oxidation, immediately prior to EBSD characterization, the samples were placed in an inert Ar glove box to minimize oxidation, and they underwent a polishing to mechanically remove any surface oxidation. The samples were polished down to a 1 µm surface finish using alumina paste, and were subsequently placed in a vibratory polisher with 0.05 µm diamond solution for several hours. Care was then taken to minimize the samples exposure to air during transfer from the glovebox into the SEM. The EBSD patterns were collected at 20KV using 0.3 to 0.5µm step sizes. Long exposure times, at approximately 75% of the maximum, with low signal gain were used to improve data collection.

Inverse Pole Figure (IPF) maps, confidence maps, and grain-size-plots were generated. The IPF and confidence maps presented in this manuscript are composite micrographs with the IPF and confidence maps superimposed. In the resulting micrographs, brighter and darker regions represent areas of high and low confidence, respectively. Areas that appear near black represent regions of very low confidence that likely indicate the presence of secondary phases such as U oxides or carbides that were not considered in the analysis. The grain-size-plots display the grain sizes as calculated by the EBSD software.

Fractography of selected specimens was performed by SEM analysis to determine the failure mechanisms, and where possible to determine fracture initiation locations. No further reporting on this is performed as part of this study.

2.3.5 Calculated Strength Uncertainties

The overall uncertainty in specimen strength calculations is a function of accuracy of specimen pre-test dimensional measurement (inconsequential in these tests) and measured force errors. Additionally, linearity of strain transducer response and, to a lesser degree, the absolute accuracy of the measured strain values influences the yield strength determinations.

Standard deviation for yield stress and ultimate tensile stress for each group of specimens was calculated. The standard deviation of calculated strength values for replicate specimen groups are reported in the results section. Standard deviations are typically 8–14 MPa, with a low value of zero (perfect specimen-to-specimen agreement); two UTS groups were approximately 65–80 MPa. In essence, replicate specimen-to-specimen variability seemed to be larger than combined errors introduced by force-measurement inaccuracies.

2.4 Results

2.4.1 Metallography of the as-rolled material

The following micrographs (see Figure 1), produced from polished met mounts of material tested to failure in this work, reveal both notable carbide precipitates in long strings throughout the base material and cracks that propagate along the carbide strings. The carbide precipitates range in size from 1–2 µm up to 10 µm and are a consequence of the high carbon content, ~710 ppm, noted in Table 2.2. Using the model developed by Devaraj et al (2016) [33], this amount of carbon content from the chemistry analysis, results in a volume fraction of uranium carbide in the alloy of ~1.86%. Backscatter images show the presence of lighter and darker regions (atomic number contrast or Z contrast) which are variations in the Mo content and are referred to as Mo banding [34, 35].

EBSD micrographs are shown in Figure 2 along with plots of the grain size distribution. Although the collected EBSD data shows regions with low confidence, the collected data is sufficient to determine the grain size for each of the foil conditions except for 551-2-2

50%CW in which significant regions of low confidence were present. Thus, the collected data may not be representative of the microstructure.

In 551-2-2-L11 50%CW the Mo banding varies between 8.35 wt% and 10.45 wt% and demonstrates carbide precipitate strings and cracks along the carbide strings. Significant portions of the collected data for this sample exhibited low confidence. Thus, the collected data may not be representative of the samples' microstructure. Grain sizes for the longitudinal and transverse cross-sections ranged from 2 to 22 µm with the greatest concentration between 15 and 18 µm for the longitudinal direction and between 7 and 8 µm for the transverse direction.

In 551-3-L30 50%CW+A, the Mo banding ranges from 8.96 wt% to 10.81 wt%. Formation of carbide strings are less evident than when compared to the 50%CW case and no obvious crack propagation is noted in the image. This may be a result of the annealing treatment. Grains in the range between 2 to 12 µm with the greatest concentration of grain sizes between 5 to 9 µm for both the longitudinal and transverse directions). The grains in this microstructure do not appear to show significant grain elongation. The grains in this microstructure appear more equiaxed. Presumably new grain growth has taken place.

In 551-4-L14 20%CW the Mo banding ranges from 9.81 wt% to 10.45 wt% and the formation of carbide precipitates into long strings seems less apparent in this material than when compared to the other foil material included in this study. Grains between 2 to 25 µm with the greatest concentration of grains between 7 to 17 µm for both the longitudinal and transverse directions). The grains in this microstructure do appear to show elongation.

Finally in 551-5-L13 HR Only the Mo ranges from 8.46 wt% to 10.41 wt%. The carbides in this specimen do not form the obvious strings when compared to the other materials included in this study, but did form larger precipitates when compared to the other material in this study. Grains between 2 and 22 µm with the greatest concentration in the longitudinal sample being 20 µm and the greatest concentration in the transverse sample being between 7 and 10 µm. The grains in this microstructure appear to show some grain elongation. Elongation of the grains in the longitudinal direction make indicate the microstructure may have retained residual stresses from the rolling process

551-2-2-L11 50%CW

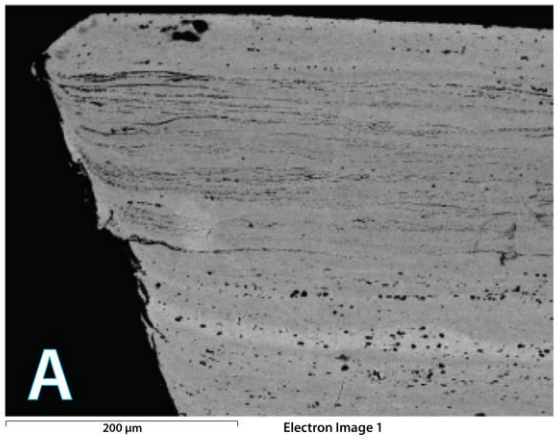

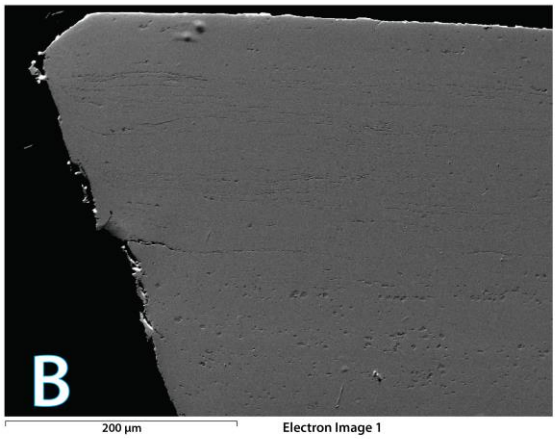

551-3-L30 50%CW+A

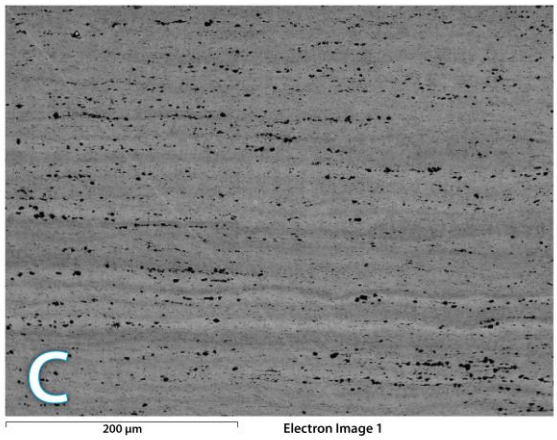

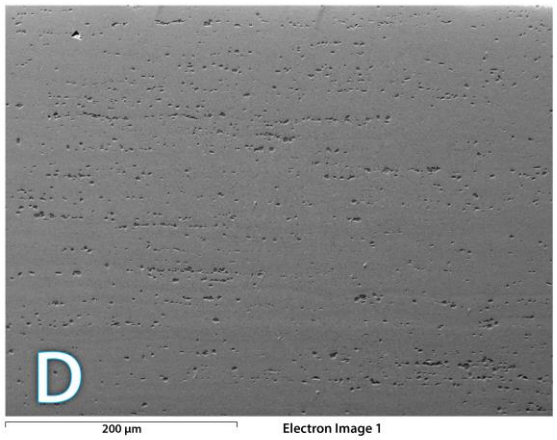

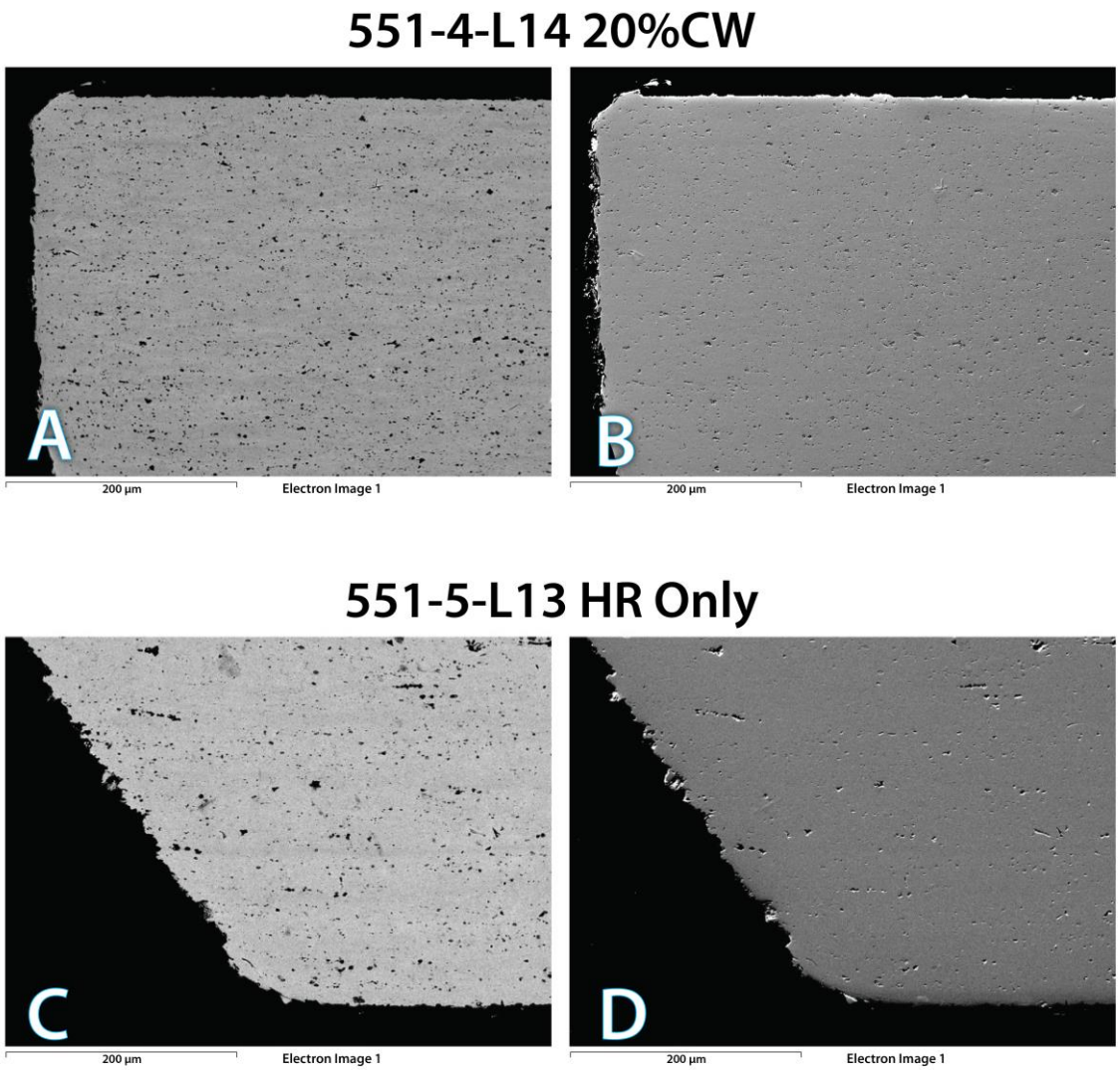

Figure 2.1 This figure shows representative metallography of all four-foil conditions. 551-2-2-L11 50%CW, A) Back scattered electron image (BSE) showing carbide precipitate strings, and Mo banding. B) Secondary image (SE): 551-3-L30 50%CW+A, C) BSE image, formation of carbide strings is less evident, possibly a result of the annealing treatment. Mo banding visible. **D)** SE image. **551-4-L14 20%CW. E)** BSE image, carbide precipitates continue to be present along with Mo banding and there is less formation of carbide strings. **F)** SE image; **551-5-L13 HR Only. G)** Similar to 551-1-L14 20%CW **H)** SE image.

551-2-2-L11 50%CW

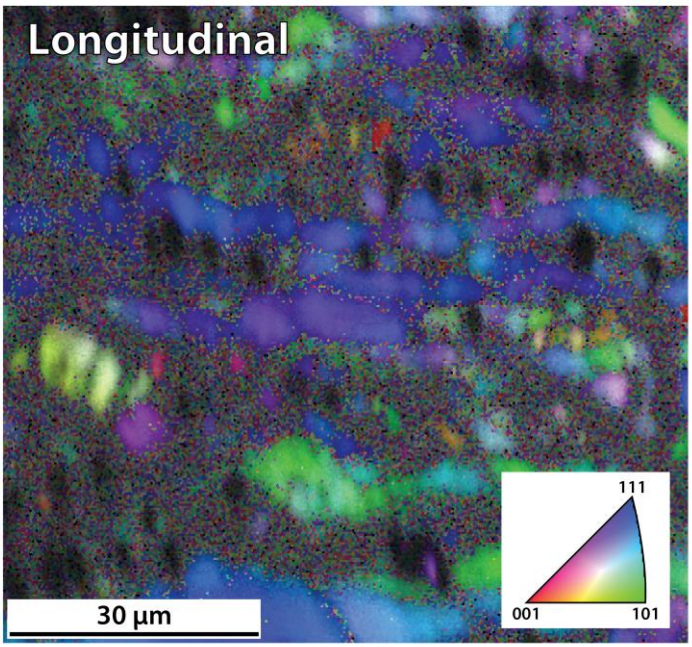

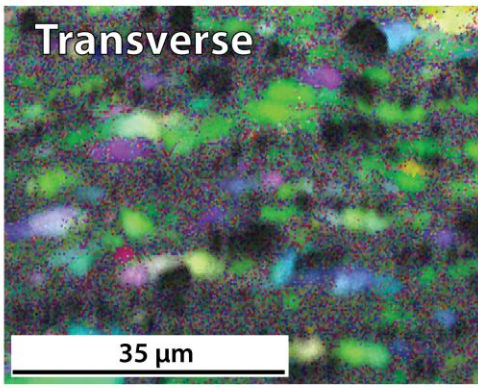

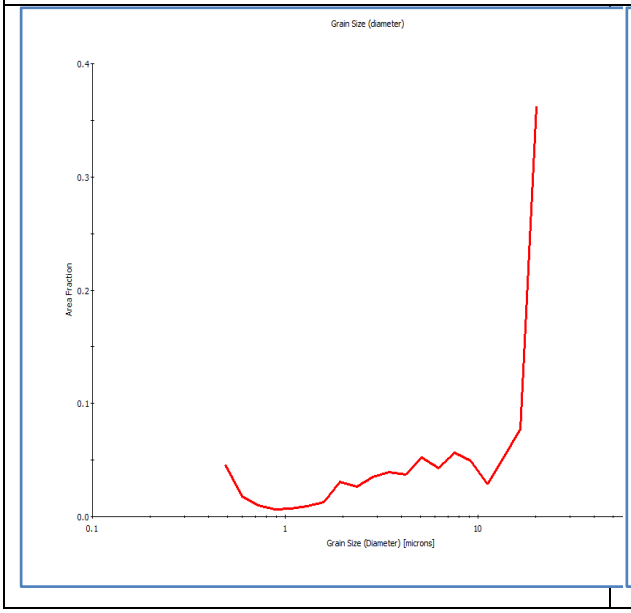

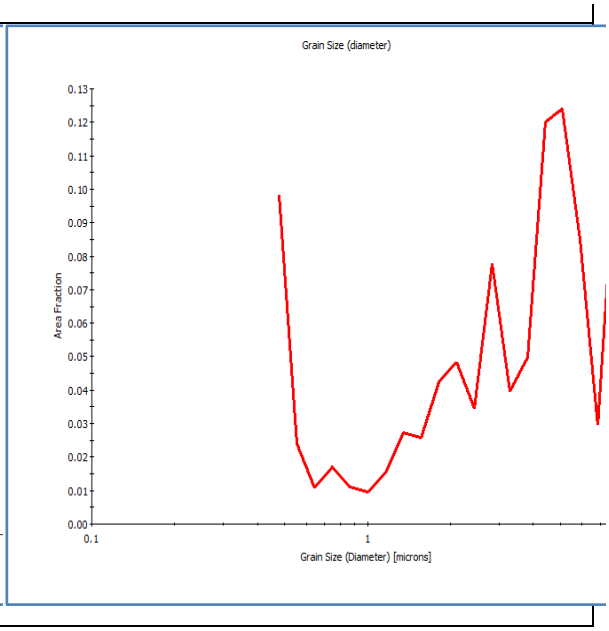

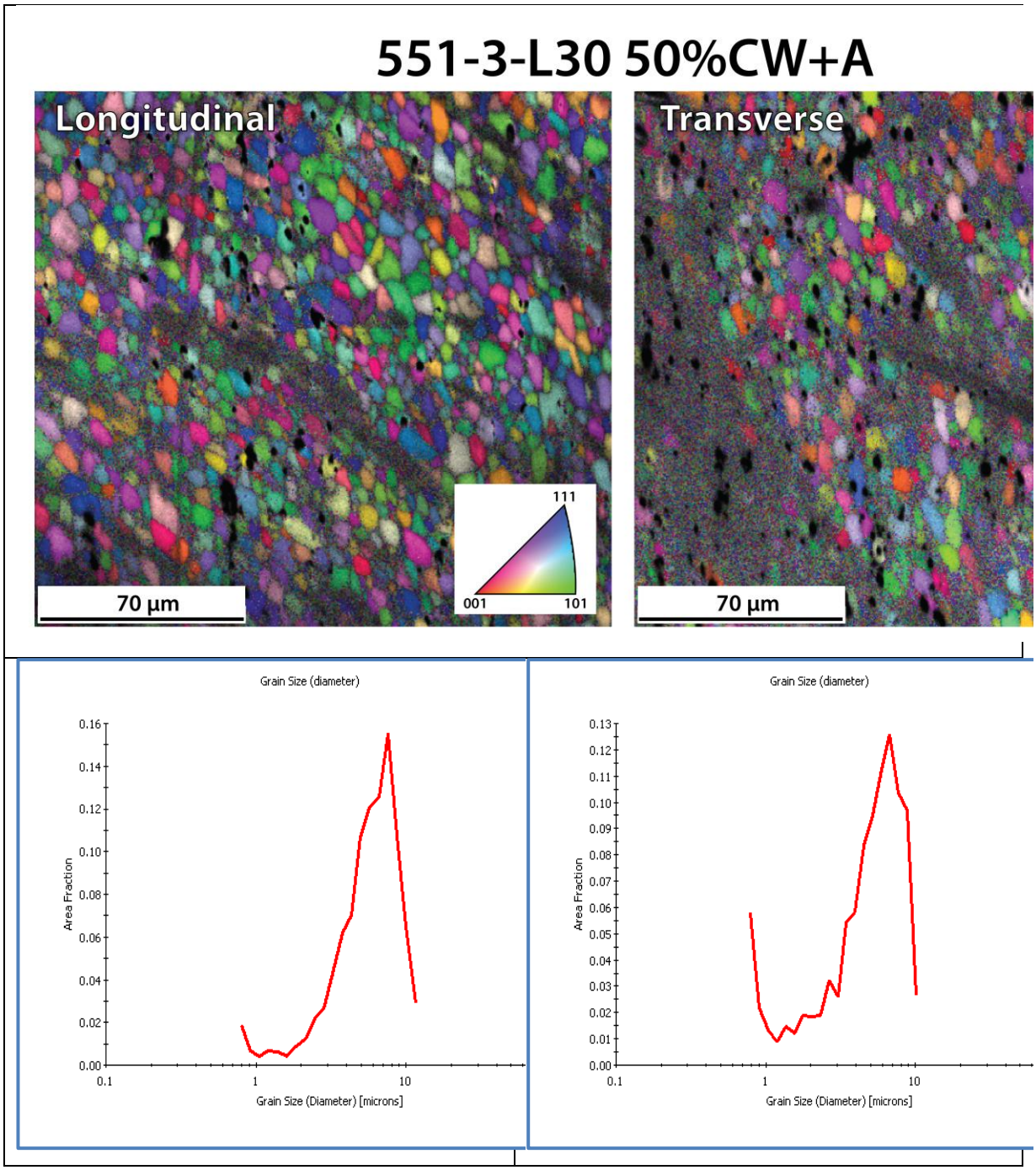
551-3-L30 50%CW+A
Longitudinal
Transverse
111
001
101
70 µm
70 µm
Grain Size (diameter)
Area Fraction
Grain Size (Diameter) [microns]
Grain Size (diameter)
Area Fraction
Grain Size (Diameter) [microns]

551-4-L14 20%CW

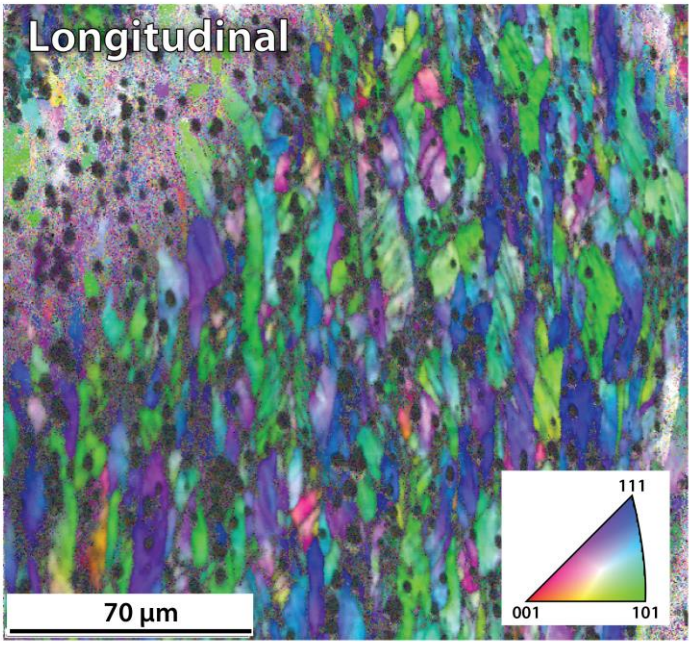

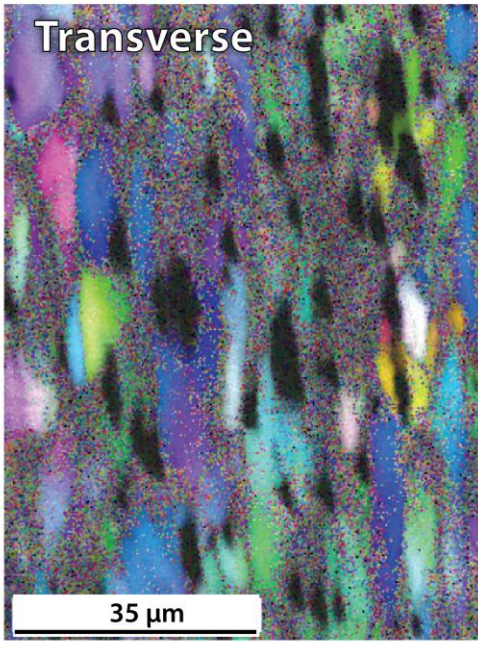

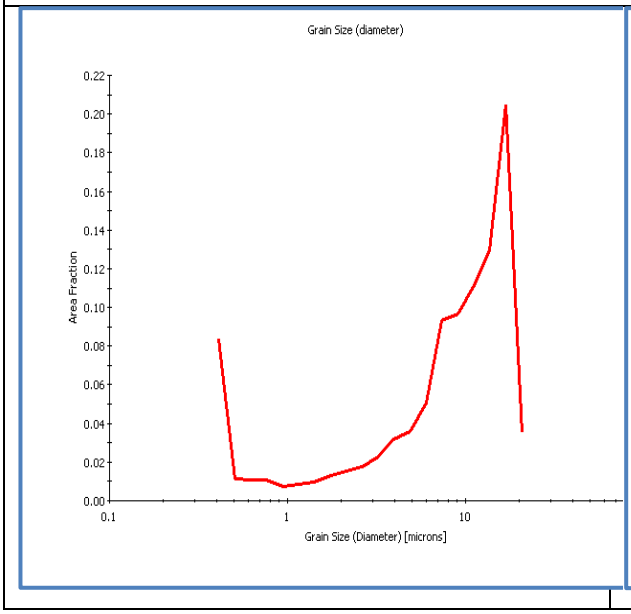

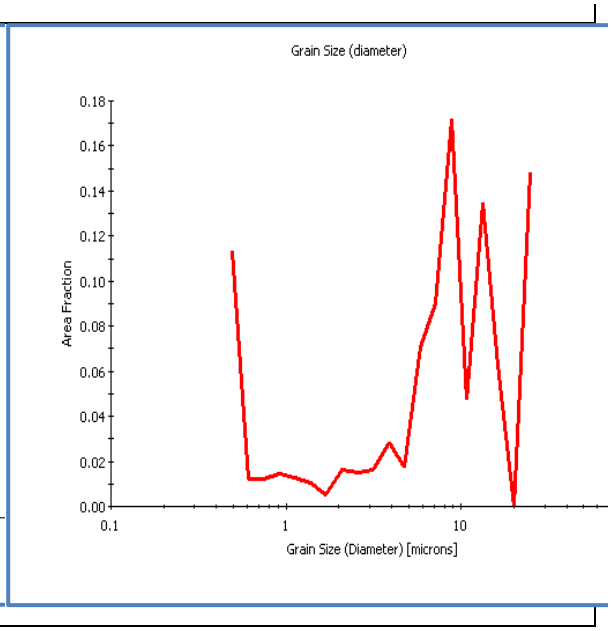

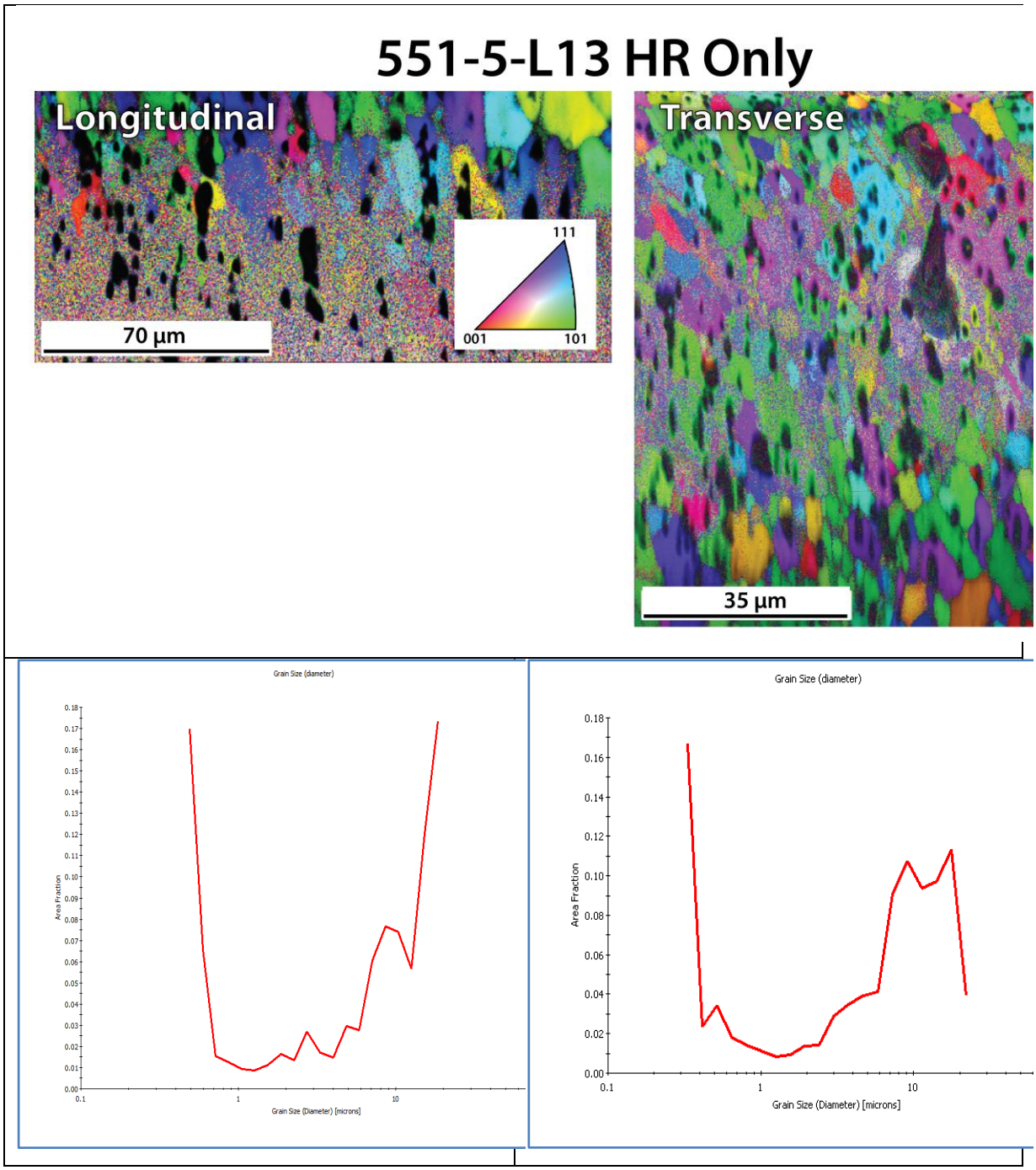

Figure 2.2. EBSD images from grain size analysis of foil conditions. Longitudinal and transvers images are shown for each foil condition along with a plot of the grain size distribution. In each of the foil conditions, significant regions of high confidence with EBSD analysis were found giving confidence to the analysis, except for foil 551-2-2 50%CW in which significant regions showed low confidence. Thus, the collected data for 551-2-2 50% CW may not be representative of the microstructure. The black spots in the images are artifacts from difficulties in cleaning the specimens during sample preparation. Multiple attempts and methods were made to reduce and eliminate these spots but were ultimately unsuccessful in completely removing them.

Table 2.3. Summary of mechanical properties from the current work.

Group Identifier	Condition	Orientation	Nominal T (°C)	Avg YS (MPa)	Std.Dev. YS (MPa)	Avg. UTS (MPa)	Std.Dev. UTS (MPa)	Avg Elongation (%)	Std. dev. Elongation (%)
551-2-2-L-20	50% CW	L	20	1108	8	1172	5	2.9	1.2%
551-2-2-T-20	50% CW	T	20	1084	14	1111	62	1.2	0.8%
551-3-L-20	50% CW + A	L	20	1012	1	1015	1	8.9	0.2%
551-3-T-20	50% CW + A	T	20	1029	1	1030	2	7.3	0.3%
551-4-L-20	20% CW	L	20	1105	15	1151	12	5.9	0.2%
551-4-T-20	20% CW	T	20	1063	6	1139	38	1.6	0.5%
551-5-L-20	HR ONLY	L	20	1043	18	1014	6	11.7	0.8%
551-5-T-20	HR ONLY	T	20	1025	0	1033	19	2.9	2.9%
551-3-L-200	50% CW + A	L	200	662	8	710	2	13.5	0.5%
551-3-T-200	50% CW + A	T	200	678	2	725	2	13.4	1.8%
551-4-L-200	20% CW	L	200	869	4	914	2	2.9	0.1%
551-4-T-200	20% CW	T	200	799	15	934	28	3.1	1.0%
551-5-L-200	HR ONLY	L	200	663	2	717	13	8.1	3.6%
551-5-T-200	HR ONLY	T	200	696	4	723	10	3.2	1.2%
551-2-2-L-250	50% CW	L	250	868	22	941	23	2.7	0.8%
551-2-2-T-250	50% CW	T	250	860	4	860	29	1.6	0.3%
551-2-2-L-350	50% CW	L	350	793	28	880	4	4.1	0.3%
551-2-2-T-350	50% CW	T	350	NA	NA	593	80	0.6	0.4%

Group Identifier	Condition	Orientation	Nominal T (°C)	Avg YS (MPa)	Std.Dev. YS (MPa)	Avg. UTS (MPa)	Std.Dev. UTS (MPa)	Avg Elongation (%)	Std. dev. Elongation (%)
551-3-L-400	50% CW + A	L	400	487	4	564	5	4.9	1.0%
551-3-T-400	50% CW + A	T	400	497	6	574	4	5.8	0.5%
551-4-L-400	20% CW	L	400	616	5	715	4	2.6	0.2%
551-5-L-400	HR ONLY	L	400	494	2	610	4	9.3	0.9%
551-2-2-L-450	50% CW	L	450	520	19	606	7	9.0	0.6%
551-2-2-L-550	50% CW	L	550	137	2	169	5	73.3	7.2%
551-2-2-T-550	50% CW	T	550	99	13	144	25	42.2	6.3%
551-3-L-550	50% CW + A	L	550	165	6	200	2	69.1	6.5%
551-3-T-550	50% CW + A	T	550	162	2	197	5	65.6	2.4%
551-4-L-550	20% CW	L	550	152	6	193	6	45.9	3.3%
551-4-T-550	20% CW	T	550	153	4	192	8	33.7	7.2%
551-5-L-550	HR ONLY	L	550	229	2	269	2	39.7	3.7%
551-5-T-550	HR ONLY	T	550	199	7	274	5	46.2	0.9%

2.4.2 Mechanical Properties

Average results from all of the valid tests from both longitudinal and transverse tensile specimens are presented for both room-temperature and elevated-temperature tests (see Table 2.3). A plot of typical stress-vs.-strain curves from each foil condition tested, at each of the temperatures tested is provided in Figure 3. A summary plot of the yield stress results for longitudinally oriented specimens is provided in Figure 4. The ultimate tensile stress in the longitudinal orientation as well as the yield and ultimate stress in the transverse orientation follow a similar trend. The elongation results are visualized in Figure 5. There is a notable increase in elongation when the test temperature reaches 550°C, compared to those seen at lower test temperatures.

Given the small size of the test specimens, which tend to increase specimen-to-specimen variation in measured properties, the results are reasonably consistent. Small scale specimens are more sensitive to a number of factors including the relative size of the grains to the cross section of the specimen, the size and distribution of defects relative to the cross section of the specimen, and test system alignment. Alignment, in particular, is of concern with small samples as the induced bending moment in the small specimen has a greater effect than it would in a large, standard size specimen. [36]

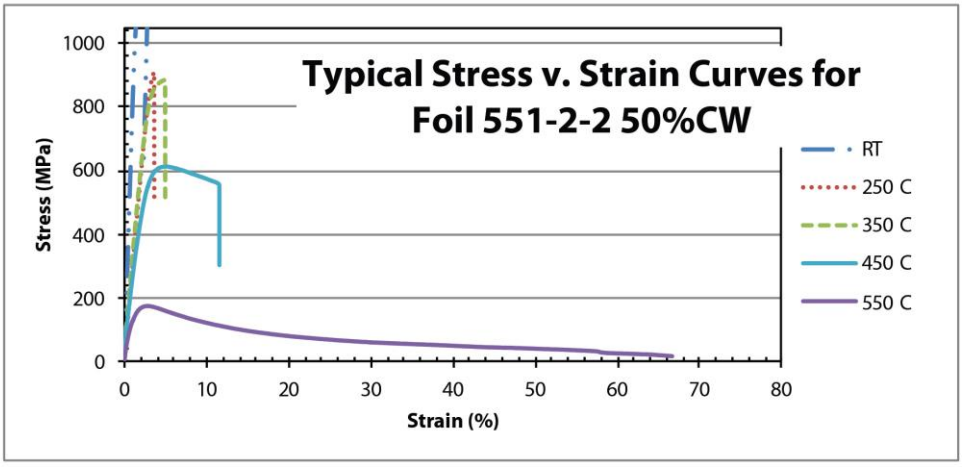
Typical Stress v. Strain Curves for
Foil 551-2-2 50%CW
Stress (MPa)
Strain (%)
RT
250 C
350 C
450 C
550 C

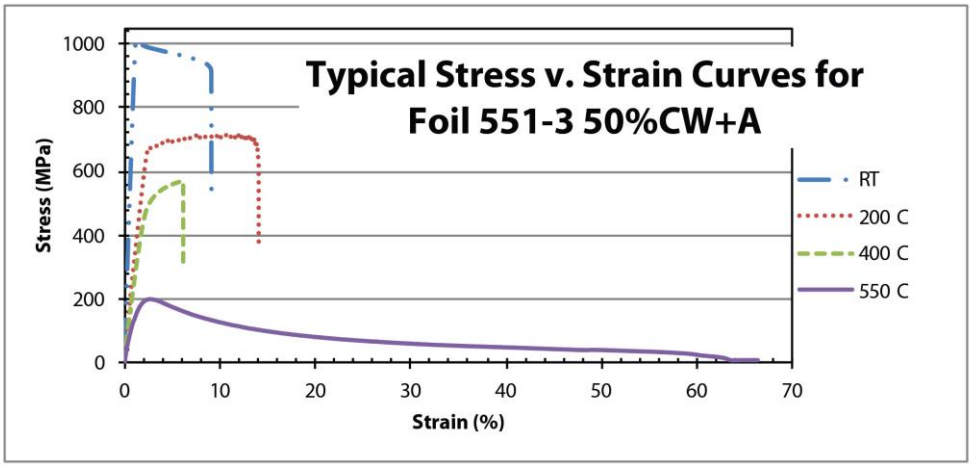
Typical Stress v. Strain Curves for
Foil 551-3 50%CW+A
Stress (MPa)
Strain (%)
RT
200 C
400 C
550 C

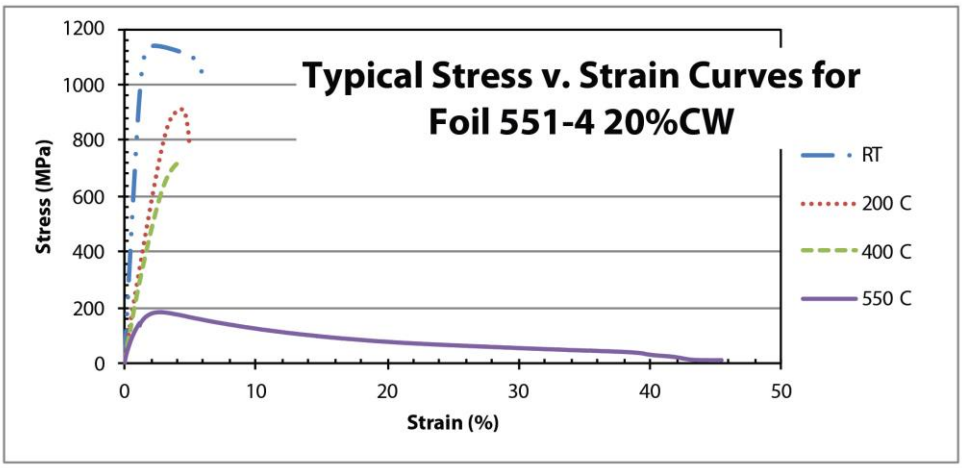

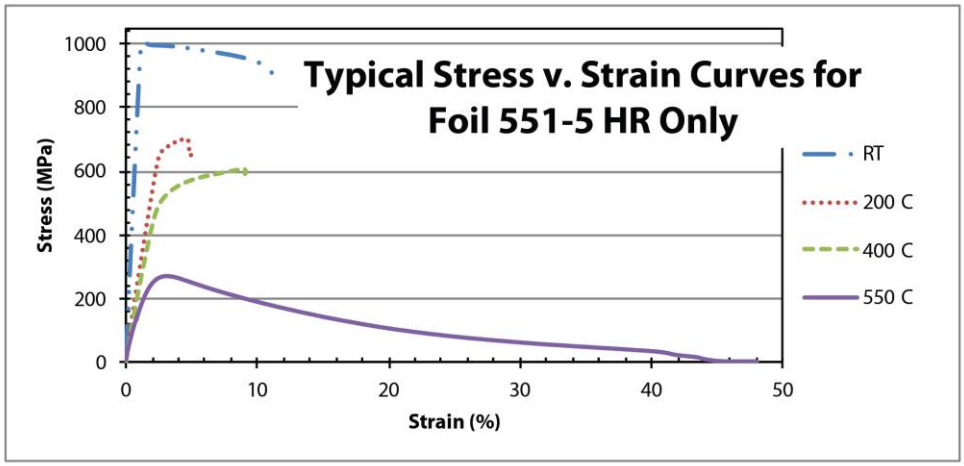

Figure 2.3. Typical Stress v. Strain curves for each foil condition for each temperature tested.

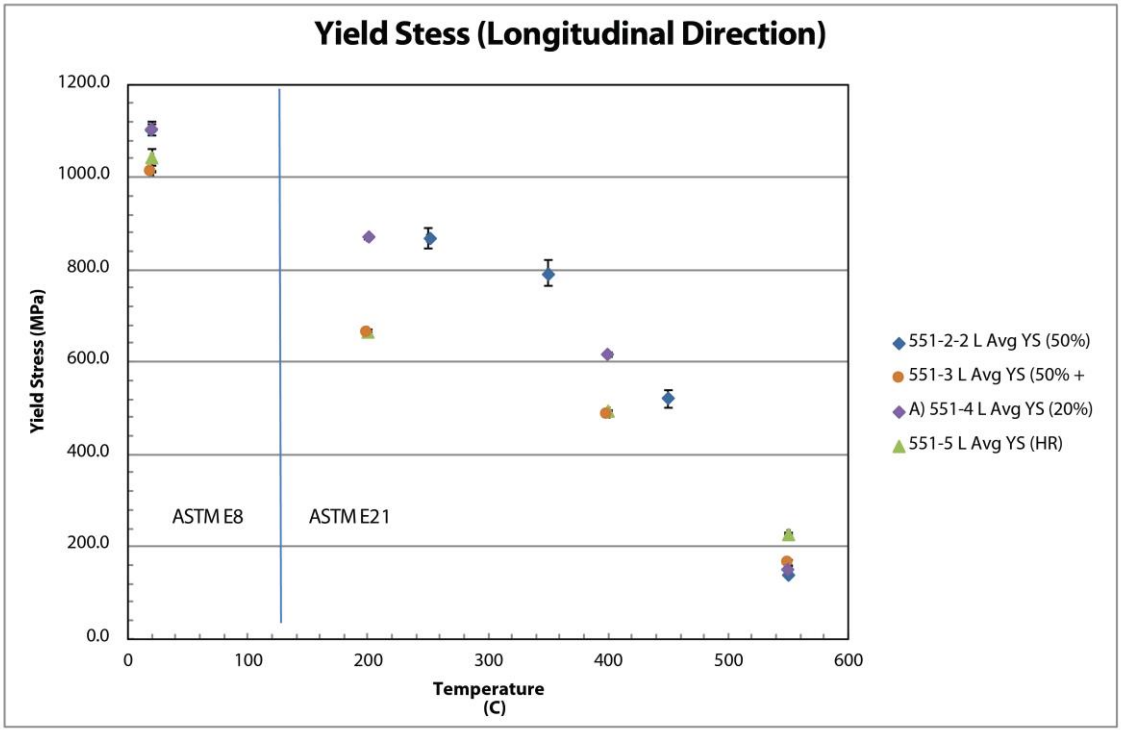

Figure 2.4. Yield stress in the longitudinal direction for each of the four foil fabrication conditions. The figure shows the cluster of yield stress at room temperature and at 550°C while there is a divergence in the fabrication conditions in the intermediate values. The annealed and hot-rolled-only foils indicate lower yield stress values in the intermediate temperatures. Where error bars are not visible, the error is small enough to be obscured by the plot marker.

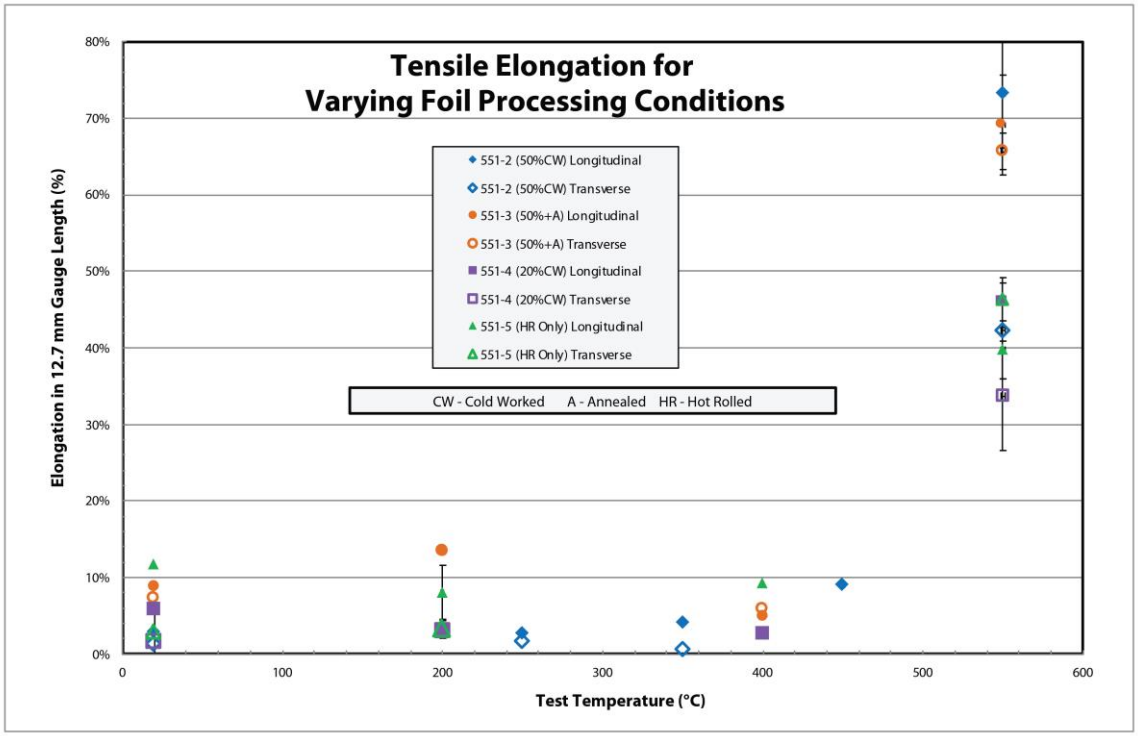

Figure 2.5. Elongation for all foil conditions tested. Note the significant increase in elongation when tested at 550 °C. Where error bars are not visible, the error is less than 1%.

2.4.2.1 551-2-2 50%CW

The yield strength for the 50%CW foil condition was ~1108 MPa when tested at room temperature. The yield strength decreased as the test temperature increased dropping to ~868 MPa at 250°C, then to ~793 MPa at 350°C, ~520 MPa at 450°C, and finally ~137 MPa at 550°C.

Similar results were observed for the ultimate tensile strength of the 50%CW foil, where the strength was ~1172 MPa at room temperature and decreased to ~941 MPa at 250°C, ~880 MPa at 350°C, ~605 MPa at 450°C, and ~168 MPa at 550°C.

Ductility for the 50%CW foil was measured to be ~2.9% at room temperature, decreased slightly to ~2.7% at 250°C, increased to ~4.1% at 350°C, increased again to ~9.0% at 450°C, then increased significantly to ~73.3% at 550°C.

2.4.2.2 551-3 50%CW+A

The yield strength for the 50%CW+A foil condition was ~1012 MPa when tested at room temperature. The yield strength decreased as the test temperature increased dropping to ~662 MPa at 200°C, then to ~487 MPa at 400°C, and finally ~165 MPa at 550°C.

Similar results were observed for the ultimate tensile strength of the 50%CW+A foil, where the strength was ~1015 MPa at room temperature and decreased to ~710 MPa at 200°C, ~564 MPa at 400°C, and ~200 MPa at 550°C.

Ductility for the 50%CW+A foil was measured to be ~8.9% at room temperature, increased to ~13.5% at 200°C, decreased to ~4.9% at 400°C, then increased significantly to ~69.1% at 550°C.

2.4.2.3 551-4 20%CW

The yield strength for the 20%CW foil condition was ~1105 MPa when tested at room temperature. The yield strength decreased as the test temperature increased dropping to ~869 MPa at 200°C, then to ~616 MPa at 400°C, and finally ~152 MPa at 550°C.

Similar results were observed for the ultimate tensile strength of the 20%CW foil, where the strength was ~1151 MPa at room temperature and decreased to ~914 MPa at 200°C, ~715 MPa at 400°C, and ~193 MPa at 550°C.

Ductility for the 20%CW foil was measured to be ~5.9% at room temperature, decreased to ~2.9% at 200°C, decreased to ~2.6% at 400°C, then increased significantly to ~45.9% at 550°C.

2.4.2.4 551-5 HR Only

The yield strength for the HR only foil condition was ~1043 MPa when tested at room temperature. The yield strength decreased as the test temperature increased dropping to ~663 MPa at 200°C, then to ~494 MPa at 400°C, and finally ~229 MPa at 550°C.

Similar results were observed for the ultimate tensile strength of the HR only foil, where the strength was ~1014 MPa at room temperature and decreased to ~717 MPa at 200°C, ~610 MPa at 400°C, and ~269 MPa at 550°C.

Ductility for the HR only foil was measured to be ~11.7% at room temperature, decreased to ~8.1% at 200°C, increased to ~9.3% at 400°C, then increased significantly to ~39.7% at 550°C.

2.4.3 Fractography

The following micrographs, Figures 6 through 8, reveal the characteristic spherical dimples that are indicative of the ductile- or dimple-rupture failure mechanism. Note that as the test temperatures increase, the simple spherical dimples become elongated, indicative of ductile tearing. Failures also seem to be predominantly intergranular, with minor indications of transgranular failure [37] and [38].

The fractography images are presented as a series of sets. Set one (Figure 6) shows progression of the facture surface as test temperature increases for a single foil condition (551-3 50%CW+A). Set two (Figure 7) shows the facture surface for the different foil conditions which were tested at room temperature (Different foil conditions, all tested at room temperature. Set three (Figure 8) shows the fracture surface for all of the different foil conditions which were tested at 200°C (all foil conditions tested at elevated temperature (200 °C).

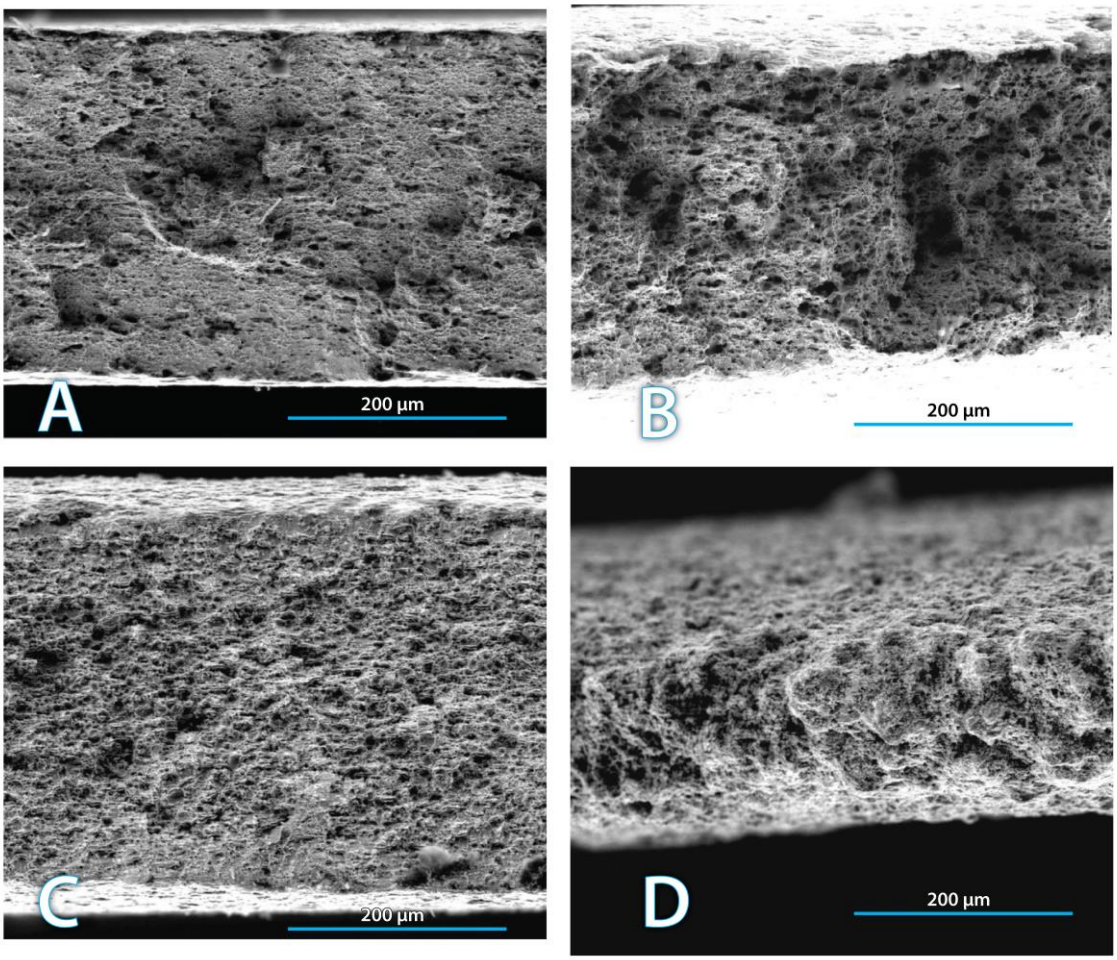

Figure 2.6. Fractography images set one. One foil condition (551-3 50%CW+A) at all test temperatures. **A)** 551-3-L1, tested at room temperature, **B)** 551-3-L4, tested at 200 °C, **C)** 551-3-L7, tested at 400 °C, **D)** 551-3 L10, tested at 550 °C.

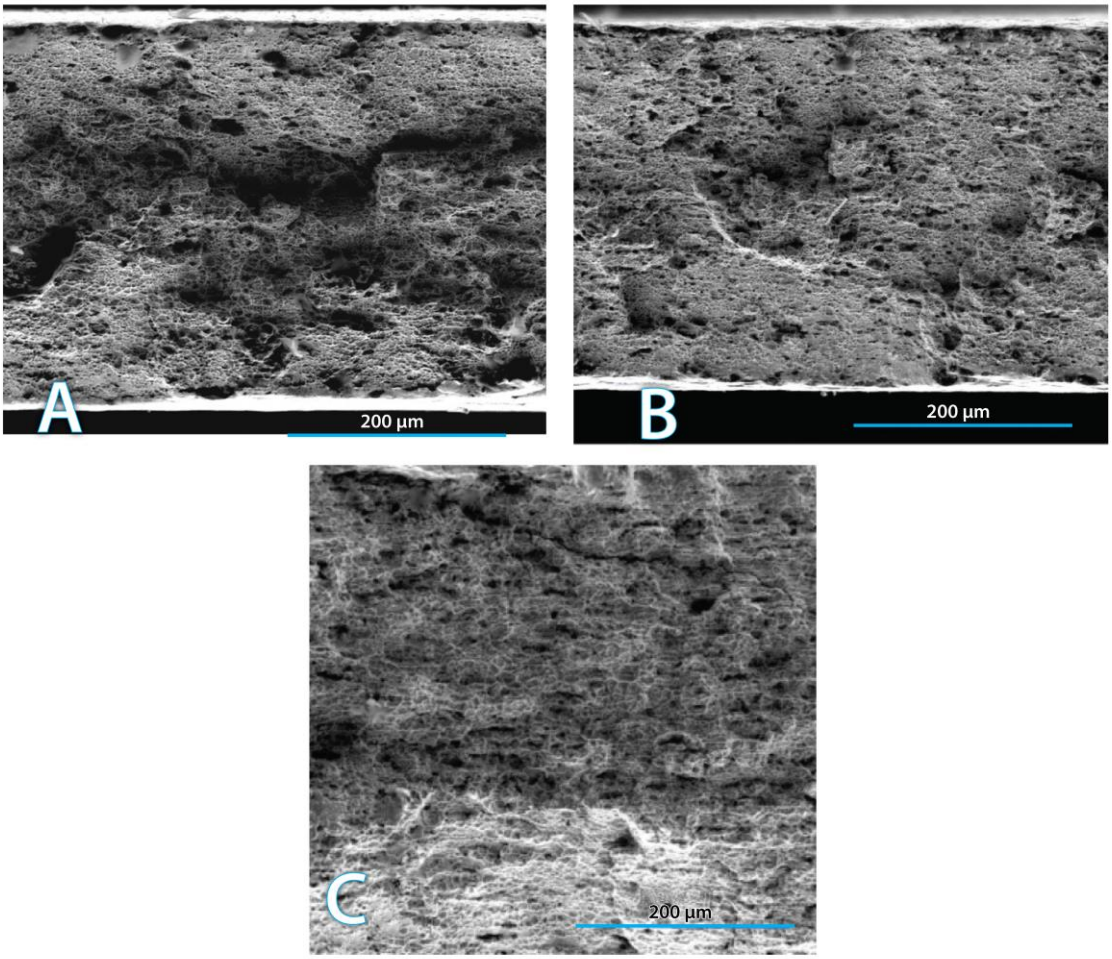

Figure 2.7. Fractography images set two. Different foil conditions, all tested at room temperature. **A)** 551-2-2-L16-RT (50%CW), **B)** 551-3-L1-RT (50%CW+A), **C)** 551-5-T13-RT.(HR only).

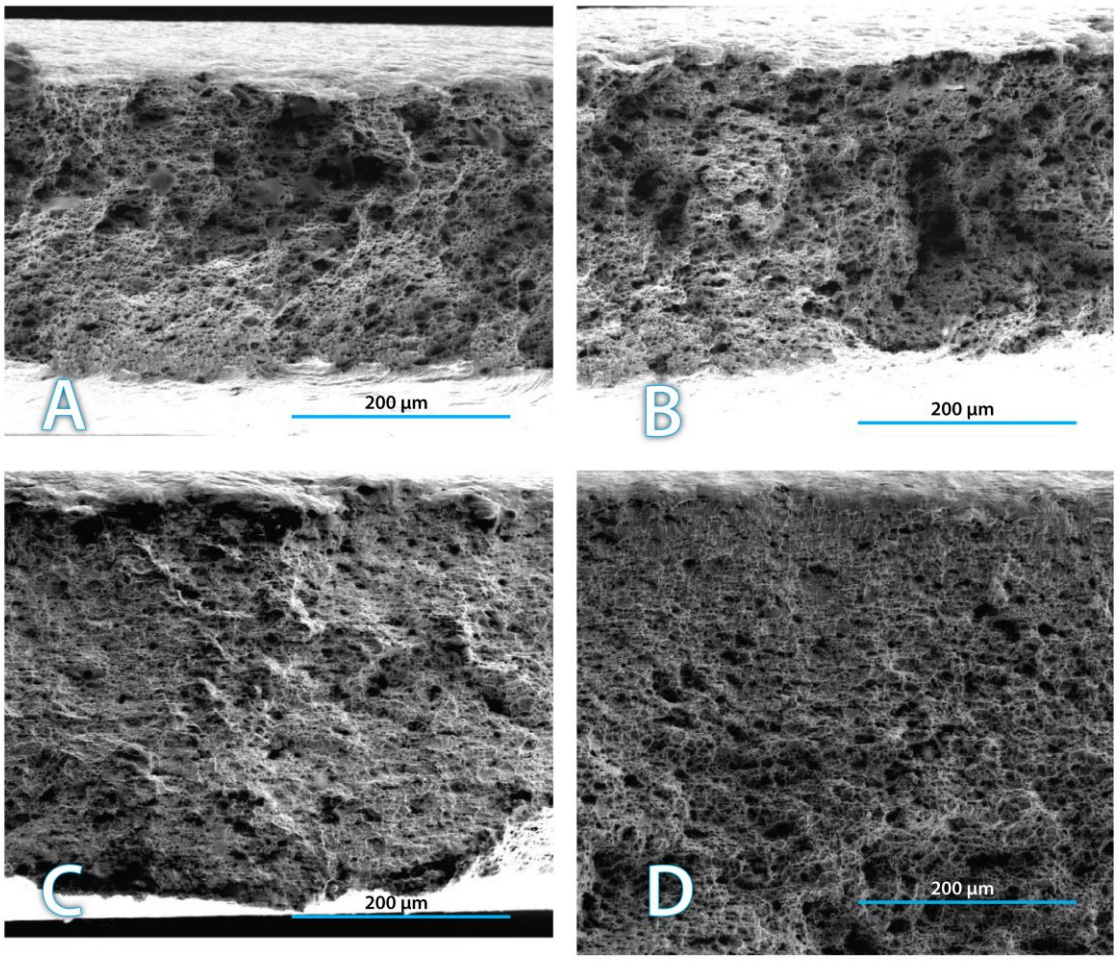

Figure 2.8. Fractography images set three, all foil conditions tested at elevated temperature (200 °C). **A)** 551-2-2-L20-200 (50%CW), **B)** 551-3-L4-200 (50%CW+A), **C)** 551-4-L5-200 (20%CW), **D)** 551-5-L4-200 (HR only).

2.5 **Discussion**

Tensile properties of DU–10Mo at room temperature through approximately 400°C, determined from the tests conducted herein, suggest the material is stronger and has greater ductility than what has been reported previously in the literature for U-10Mo alloys. Generally, for this work, the yield stress for all foil processing conditions was found to be in the range of 1100 MPa for room temperature tests. Ultimate tensile stress was in the range of 1175 MPa at room temperature. As noted previously, Waldron [5] reported UTS values at room temperature at ~617 MPa, while Ozaltun [7] reported UTS at room temperature at ~790 MPa. This indicates that the material tested in this work, with respect to UTS, is stronger than the material of Waldron [5] and Ozaltun [7] by 558 MPa and 385 MPa respectively.

Likewise, the elongation of this work increased significantly from 1–2% at room temperature, to 50% or more for the tests at 550°C. The work by Waldron [5] and Kalashnikov [14] indicated elongation increasing from 0.1% at room temperature, to less than 1% at 600°C, to 30% when tested at 800°C. This indicates that the material tested in this work is more ductile than that of Waldron [5] and Kalashnikov [14], especially at 550°C where the elongation difference is ~50% greater for this work.

The explanation for these differences of yield, UTS, and elongation has yet to be determined, but is likely related to differences in grain size and/or impurity content, brought about by differences in thermomechanical processing histories. Since parameters such as grain size are not reported in sources such as Waldron [5], the results between this work and Waldron [5] cannot be conclusively compared. U-10Mo alloys are not a commercially produced high volume product like aluminum 6061 that is fabricated to a tight specification. It is possible that small variations from heat to heat of U-10Mo and feedstock differences could account for part of the observed differences.

At the highest temperatures tested (550°C) better agreement between the values reported here, yield stress in the range of 200 MPa for tests conducted at 550°C and UTS approximately 225 MPa at 550°C, and that reported in the available literature was found. Waldron [5] and Kalashnikov [14] reported UTS between 124 and 194 MPa when tested at 600°C, resulting in a difference of less than 100 MPa.

Since the thermomechanical processing histories between the material reported in this work and that reported previously in the literature is different, no further comparisons between the data will be made. Rather, additional details on the observed effects of the different foil processing conditions and specimen orientation on tensile properties evaluated in this work are discussed below.

The test results show good specimen-to-specimen consistency with the exception of transverse tests of foil 551–5 at room temperature. In this case, the results of one specimen were further than one standard deviation below the other tests. One additional test was performed for this condition, which agreed with the primary cluster of results and implies that the one test with low-strength results may have had an uncharacteristic failure mechanism causing premature failure.

2.5.1 Yield Strength

No significant effect of fabrication history on yield stress was observed at the lowest temperature (room temperature) and highest temperature (550°C) tested. At room temperature, the yield strength of each foil condition was: 551-2-2 50%CW ~1107 MPa; 551-3 50%CW+A ~1012 MPa; 551-4 20%CW ~ 1105 MPa; 551-5 HR Only ~1043 MPa. The maximum difference between these values is ~95 MPa. At 550°C, the yield strength of each foil condition was: 551-2-2 50%CW ~138 MPa; 551-3 50%CW+A ~166 MPa; 551-4 20%CW ~ 152 MPa; 551-5 HR Only ~229 MPa. The maximum difference between these values is ~91 MPa.

However, tests indicated yield strength differences exist at the intermediate temperatures tested with the 50% cold-worked and annealed, and hot-rolled only material grouping together and producing lower yield stress (~663 MPa at the 200-250°C test temperature range) compared to the yield stress (~869 MPa) of the 20% cold worked and 50% cold worked foils, which were also very closely grouped. This results in a difference of yield stress between the stronger conditions (20%CW and 50%CW) and weaker conditions (50%CW+A and HR Only) of ~206 MPa.

A similar observation was made for tests conducted near 400°C, where the foils with 50%CW and 20%CW produced higher yield strength than the 50%CW+A and the HR Only foils. The specific yield strengths observed were 50%CW at 350°C yield strength was 793 MPa, 50%CW at 450°C yield strength was 520 MPa, 20%CW at 400°C yield strength was 616

MPa. For the weaker foils the strengths observed were 50%CW+A at 400°C yield strength was 487 MPa, and for the HR only foil at 400°C the yield strength was 494 MPa. This results in a difference of ~170 MPa between the strongest (50%CW) and weakest (50%CW+A) at the 400°C test temperature. Another observation we can make here is that all foil conditions experience a strong downward trend in yield strength between 350°C and 400°C.

Significant effects of specimen orientation (anisotropy due to rolling) on yield strength were only observed in a few cases (specifically, 20% cold-worked material tested at 200°C resulted in lower yield stress in the transverse orientation (~799 MPa) compared to the longitudinal orientation (~869 MPa). An orientation effect was also observed in the 20% cold-worked material at room temperature, where the transverse yield was ~1063 MPa and the longitudinal is ~1105 MPa. Finally, the orientation effect was observed in the 50% cold-worked case at room temperature with the transverse yield being ~1084 MPa, and the longitudinal yield being ~1107 MPa. While this orientation effect is observed at the lower test temperatures, it is only observed in the cold-worked foil conditions and the effects are not large in magnitude. The effect also dissipates at the higher test temperatures, which may be indicative of some stress relief occurring due to the exposure to temperature.

2.5.2 Ultimate Tensile Strength (UTS)

Significant differences in the UTS were noted in the longitudinal direction for the four foils at room temperature, with the difference continuing, but converging as the temperature increased. This difference between each of the four foils was also found to exist in the transverse direction. Both the 50% cold-worked and annealed and hot-rolled only material produced lower ultimate tensile stress (~1015 MPa, ~1014 MPa respectively) at room temperature compared to the 50% cold-worked and 20% cold-worked material (~1172 MPa, ~1151 MPa respectively), for a difference of ~158 MPa.

As stated, near the 200°C test temperature, this difference in UTS continued between the 4 foil conditions where the UTS was observed to be 50%CW at 250°C ~941 MPa, 20%CW at 200°C ~914 MPa, 50%CW+A at 200°C ~710 MPa, and HR Only at 200°C ~717 MPa. The maximum difference in strength observed in this test temperature range was ~231 MPa.

The differences in UTS continued into 400°C test temperature range; but became smaller in magnitude. The UTS for each foil condition was observed to be: 50%CW at 350°C ~880 MPa, 50%CW at 450°C ~605 MPa, 20%CW at 400°C ~715 MPa, 50%CW+A at 400°C ~564

MPa, HR Only at 400°C ~610 MPa. Thus the maximum difference in strength observed in this test temperature range was ~178 MPa. As with the observation made in the yield strength, all foil conditions exhibited a strong downward trend in UTS between 350°C and 400°C.

Orientation effects for UTS for specimens from the same foil were only noted in the 50% cold-worked material in the following temperature cases: at room temperature, at 250°C, and at 350°C. At room temperature, the difference in UTS between longitudinal and transverse strength was ~61 MPa. At 250°C the difference was ~81 MPa. At 350°C the difference was ~287 MPa. It is currently unknown why such strong anisotropy presented in the 50% cold-worked material at the 350°C test temperature. It is recommended that this be the subject of future investigation.

All other tests indicated no significant anisotropy due to rolling direction with respect to UTS.

2.5.3 Elastic Modulus

The tension testing of this work was not conducted per ASTM E111-04 therefore, the results do not meet the requirements of ASTM E111-04 [39] for reporting modulus. Nevertheless, the slope of the initial section of the stress-strain curve was calculated for each specimen and then averaged across all specimens tested in each temperature group; resulting in an effective modulus for comparison to previously published literature data, and for understanding trends in the material properties. The average slope in MPa/% and standard deviation for each test temperature are: 20°C: 884.21±13.15; 200°C–250°C: 417.63±16.81; 350°C: 422.25±14.75; 400°C –450°C: 320.43±17.88; 550°C: 199.29±24.41.

Room-temperature elastic-modulus values reported in the literature are in the low-to-mid 80s GPa range [40, 41]—consistent with our room-temperature test results for slope of the initial section of the stress-strain curve, or the effective modulus found in this work. Additional modulus data for various temperatures were found in [5] and are summarized in Table 2.1. Some non-linearity was noted in the very early stages of the stress-strain curves (particularly at higher temperatures), it is recommended as part of a future work, that to achieve a more accurate measurement, that modulus be evaluated using the ultrasonic method of ASTM E494-10 [42].

2.5.4 Ductility

Room-temperature ductility was determined for all of the foil conditions tested. Of note, at room temperature, the 50% cold worked and annealed foil (foil 551-3) showed increased ductility (8.9%) compared to the 50% and 20% cold-worked foils (elongation 2.9% and 5.9% respectively). The hot-rolled only foil showed more ductility (elongation 11.7%) in the longitudinal direction than any other foil at room temperature but showed very little ductility (elongation 2.9%) in the transverse direction, indicating significant anisotropy at room temperature.

Ductility increased continuously for all foil conditions as testing temperature increased, and was significant for foils tested at 550°C. At 550°C, the ductility for all foil conditions and orientations increased from ~<10% to as much as ~70% in the 50% cold-worked foil in the longitudinal direction (551-2) and also ~70% for the 50% cold-worked and annealed foil (551-3) in both directions. The increase in ductility at 550°C was also pronounced for the 20% cold-worked foil, with elongation for both direction ~40%.

For a few specimens in both room temperature and elevated temperature cases, the 0.2% offset curve did not intersect the stress-strain curve. Theoretically, ductility would be very small in these cases. When combined with the measurement error evaluated in [30] and recognizing that it can be difficult to accurately piece specimens back together for post-test elongation measurements due to roughness at the fracture surface; it is likely that actual elongation values are less than the reported values of 3% or less. This specifically includes the following specimens tested at room temperature: 551-2-2 L17, and T14; 551-5 T1, and T2; and the following specimens tested at elevated temperature: 551-2-2 T11, and T5, but may impact any specimens with reported elongation values of less than 3% (see Figure 5).

At the higher temperatures tested, some strain rate effect may be present. The lack of linearity in the early portion of the test data for the high-temperature (550°C) tests, suggests that the rate of stress relaxation is close to the stress induction rate at the tested strain rate.

2.5.5 Discussion of Metallography and Fractography

The failure mechanism identified in this series of tests is ductile rupture. While no other failure mechanisms were identified, it was noted that as the test temperature increased, the fractography showed more tearing or ductile dimple rupture behavior along the fracture

surface. Combined with the increased elongation at the higher test temperatures, ~1-2% at room temp to greater than ~50% at 550°C, the more gradual failure of the specimens is to be expected.

The metallography showed a strong presence of carbide precipitates in all of the material analyzed. However, all of the material had similar carbon impurities (approximately 714 ppm) because it was sourced from the same material from Y-12 (See Table 2.2). Therefore, the effect on mechanical properties based on variations in carbon impurities, such as a lower ppm count of carbon (i.e. 400 ppm versus 714 ppm), cannot be analyzed from this data set. There was a notable difference in the presence of carbide strings between the annealed foils conditions and those foils which were not annealed. Based on the results here, the carbide strings provide a crack propagation path, and should be avoided during fabrication through annealing.

The variation in Mo content, from ~8.45 wt%Mo to ~10.46 wt%Mo, observed in the foils may be indicative that the homogenization treatment did not completely homogenize the microstructure. The impact that the homogenization of Mo content would have on the mechanical properties is unclear as all of the material tested contained such variation. It is recommended that additional testing of fully homogenized material be conducted for comparison.

2.6 References

1 J.L. Snelgrove, G.L. Hofman, M.K. Meyer, C.L. Trybus, T.C. Wiencek, “Development of very-high-density low-enriched-uranium fuels,” *Nuclear Engineering and Design,* 178 (1997) 119-126.

2 K. Daum, C. Miller, B. Durtschi, *Base Monolithic Fuel: Research, Development, and Qualification Plan,* INL/EXT-13-30238, 2014.

3 S. Hu, A.M. Casella, C.A. Lavender, D.J. Senor, D.E. Burkes, “Assessment of effective thermal conductivity in U-Mo metallic fuels with distributed gas bubbles,” *Journal of Nuclear Materials*, 462 (2015) 64-76.

4 J. Wang, X.J. Liu, C.P. Wang, “Thermodynamic modeling of the Al-U and Co-U systems,” *Journal of Nuclear Materials,* 374 (2008) 79-86.

5 M.B. Waldron, R.C. Burnett, S.F. Pugh, The Mechanical Properties of Uranium–Molybdenum Alloys, UK Atomic Energy Authority Technical Report, ARE-MB-2554, 1958.

6 A. Soulami, D.E. Burkes, V.V. Joshi, C.A. Lavender, D. Paxton, “Finite-element model to predict roll-separation force and defects during rolling of U-10Mo alloys,” *Journal of Nuclear Materials,* 494 (2017) 182-191.

7 Hakan Ozaltun, M-H., Herman Shen, and Pavel Medvedev, “Assessment of residual stresses on U10Mo alloy based monolithic mini-plates during Hot Isostatic Pressing,” *Journal of Nuclear Materials* 419 (2011), pp. 76–84.

8 H. Ozaltun, P.G. Medvedev, *Structural Behavior of Monolithic Fuel Plates During Hot Isostatic Pressing and Annealing,* Proceedings of 14th International Topical Meeting on Research Reactor Fuel Management, March 2010, Marrakech, Morocco

9 P.G. Medvedev, H. Ozaltun, A.B. Robinson, B.H. Rabin, *Shutdown-induced tensile stress in monolithic miniplates as a possible cause of plate pillowing at very high burnup,* Proceedings of 15th International Topical Meeting on Research Reactor Fuel Management, March 2014, Ljubljana, Slovenia

10 B. Rabin, M. Meyer, J. Cole, I. Glagolenko, G. Hofman, W. Jones, J.F. Jue, D. Keiser Jr, Y. Kim, C. Miller, G. Moore, H. Ozaltun, F. Rice, A. Robinson, J. Smith, D. Wachs, W. Williams, N. Woolstenhulme, *Preliminary Report on U-Mo Monolithic Fuel for Research Reactors,* INL/EXT-17-40975, 2017.

11 S.J. Miller, H. Ozaltun, *Evaluation of U10Mo Fuel Plate Irradiation Behavior via Numerical and Experimental Benchmarking,* Proceedings of ASME 2012 International Mechanical Engineering Congress and Exposition, 2012, Paper No. IMECE2012-89588, Houston, Texas.

12 H. Ozaltun, M.H. Herman Shen, P. Medvedev, S.J. Miller, “Computational evaluation for the mechanical behavior of U10Mo fuel miniplates subject to thermal cycling,” *Nuclear Engineering and Design,* 254 (2013) 165-178.

13 H. Ozaltun, *The Effects of Fabrication Induced Residual Stress-Strain States on the Irradiation Performance of Monolithic Mini-Plates,* Proceedings of ASME 2015 International Mechanical Engineering Congress and Exposition, 2015, Paper No. IMECE2015-53050, Houston, Texas.

14 V. V. Kalashnikov, V. V. Titova, G. Ia. Sergeev, A. G. Samoilov, “Uranium-molybdenum alloys in reactor construction,” *The Soviet Journal of Atomic Energy* 5.4 (1959), pp. 1315–1325.

15 Vineet V. Joshi, Eric A. Nyberg, Curt A. Lavender, Dean Paxton, Hamid Garmestani, Douglas E. Burkes, “Thermomechanical process optimization of U–10 wt% Mo – Part 1: high-temperature compressive properties and microstructure,” *J. Nucl*. *Mater.* 465 (October 2015) pp. 805–813, ISSN 0022-3115, http://dx.doi.org/10.1016/j.jnucmat.2013.10.065.

16 Vineet V. Joshi, Eric A. Nyberg, Curt A. Lavender, Dean Paxton, Douglas E. Burkes, Thermomechanical process optimization of U–10wt% Mo – Part 2: The effect of homogenization on the mechanical properties and microstructure, *J. Nucl*. *Mater.* 465 (October 2015) pp. 710–718, ISSN 0022-3115, http://dx.doi.org/10.1016/j.jnucmat.2015.07.005.

17 D.E. Burkes, R. Prabhakaran, T. Hartmann, J.F. Jue, F.J. Rice, “Properties of DU-10 wt% Mo alloys subjected to various post-rolling heat treatments, *Nuclear Engineering and Design,* 240 (2010) 1332-1339.

18 J.T. Mihalczo, *Reactivity Calibrations and Fission-rate Distributions in an Unmoderated, Unreflected U-Mo Alloy Research Reactor,* ORNL-TM-189, 1962.

19 H.A.Saller, R.F. Dickerson, W.E. Murr, *Uranium Alloys for High Temperature Application*, Rep. BMI-1098, Battelle Memorial Institute, Columbus, OH (1956) 45 pp.

20 A.M. Nominee, D. Bedere, D. Miannay, "Influence of Physio-chemical parameters on the mechanical properties of some isotropic uranium alloys”, *Physical Metallurgy of Uranium Alloys*, *Proc. Third Army Materials Tech. Conf., Vail, CO, 1974*, J. J. Burke, ed.), Brooke Hill, Chestnut Hill, MA (1976) pp. 657–700.

21 R.F. Hills, B.R. Butcher, B.W. Howlett, “The mechanical properties of quenched Uranium–Molybdenum alloys,” *J. Nucl*. *Mater.* 11 (1964) pp. 149–162.

22 K.G. Hoge, “Some mechanical properties of uranium–10 weight percent molybdenum alloy under dynamic tension loads”, *J Basic Eng* 6 (1966) pp. 509–517.

23 *Metals Handbook*, Howard E. Boyer and Timothy L. Gall, Eds., American Society for Metals, Materials Park, OH, 1985.

24 *Structural Alloys Handbook*, 1996 edition, John M. (Tim) Holt, Technical Ed; C. Y. Ho, Ed., CINDAS/Purdue University, West Lafayette, IN, 1996.

25 D.E. Burkes, R. Prabhakaran, J. Jue, F. Rice,, "Mechanical Properties of DU-xMo Alloys with x = 7 to 12 Weight Percent", *Metall. and Materials Trans. A* 40A (2009), pp. 1069–1079.

26 C.R. Clark, G.C. Knighton, M.K. Meyer, G.L. Hofman, *Monolithic Fuel Plate Development at Argonne National Laboratory,* 2003 International Meeting on Reduced Enrichment for Research and Test Reactors, 2003, Chicago, Illinois .

27 C.R. Clark, J.F. Jue, G.A. Moore, N.P. Halinan, B.H. Park, *Update on Monolithic Fuel Fabrication Methods,* 2006 International Meeting on Reduced Enrichment for Research and Test Reactors, 2006, Cape Town, South Africa.

28 M.K. Meyer, J. Gan, J.F. Jue, D.D. Keiser Jr, E. Perez, A Robinson, D.M. Wachs, N. Woolstenhulme, G.L. Hofman, Y.S. Kim, "Irradiation performance of U-Mo Monolithic Fuel," *Nuclear Engineering and Technology,* 46 (2014) 169-182.

29 G.A. Moore, M.C. Marshall, *Co-rolled U-10Mo/Zirconium Barrier-Layer Monolithic Fuel Foil Fabrication Process,* INL/EXT-10-17774, 2010.

30 J. Schulthess, *Elevated Temperature Tensile Tests on DU–10Mo Rolled Foils*, INL/EXT-14-33639, 2014

31 *Standard Test Methods for Tension Testing of Metallic Materials*, ASTM E8/8M-13a, ASTM International Annual Book of Standards, v.3.01, 2013.

32 *Standard test Methods for Elevated Temperature Tension Tests of Metallic Materials*, ASTM E21-09, ASTM International Annual Book of Standards, v.3.01, 2013.

33 A. Devaraj, R. Prabhakaran, E.J. McGarrah, V.V. Joshi, S.Y. Hu, C.A. Lavender, *Theoretical Model for Volume Fraction of UC, ^{235}U Enrichment, and Effective Density of Final U-10Mo Alloy,* PNNL-SA-117284, 2016.

34 D.E. Burkes, T. Hartmann, R. Prabhakaran, J.F. Jue, "Microstructural characteristics of DU-xMo alloys with x = 7-12 wt%," *Journal of Alloys and Compounds,* 479 (2009) 140-147.

35 J.F. Jue, T.L. Trowbridge, C.R. Breckenridge, G.A. Moore, M.K. Meyer, D.D. Keiser Jr., "Effects of heat treatment on U-Mo Fuel Foils with a Zirconium Diffusion Barrier," *Journal of Nuclear Materials,* 460 (2015) 153-159.

36 P. Hosemann, "Small-scale mechanical testing on nuclear materials: bridging the experimental length-scale gap," *Scripta Materialia,* 143 (2018) 161-168.

37 R. J. Parrington, "Fractography of metals and plastics," *Practical Failure Analysis* Volume 2 Issue 5 (2002), pp. 16-19

38 Atlas of Fractographs, Fractography, Vol 12, ASM Handbook, ASM International, 1987

39 *Standard Test Method for Young's Modulus, Tangent Modulus, and Chord Modulus,* ASTM E111-04, ASTM International Annual Book of Standards, v.3.01, 2013

40 J. E. Gates, E.G. Bodine, J.C. Bell, A.A. Bauer, G.D. Calkins, *Stress-Strain Properties of Irradiated Uranium-10 w/o Molybdenum*, BMI-APDA-638, Battelle Memorial Institute, Columbus, OH, January, 1958.

41 G. Beghi, *Gamma Phase Uranium-Molybdenum Fuel Alloys*, EUR-4053e, European Atomic Energy Community, 1968.

42 *Standard Practice for Measuring Ultrasonic Velocity in Materials,* ASTM E494-10, ASTM International Annual Book of Standards, v.3.01, 2013

3 CHAPTER 3: MECHANICAL PROPERTIES OF IRRADIATED U-MO ALLOY FUEL

"Mechanical Properties of Irradiated U-Mo Alloy Fuel." *Journal of Nuclear Materials*, Submitted (2018)

3.1 Abstract

This paper presents results of studies aimed at characterizing the mechanical properties of irradiated U-10Mo fuel in support of monolithic base fuel qualification. Mechanical properties were evaluated in four-point bending. Specimens were taken from fuel plates irradiated in the RERTR-12 and AFIP-6 Mk. II irradiation campaigns, and tests were conducted in the Hot Fuel Examination Facility (HFEF) at Idaho National Laboratory (INL). The monolithic fuel plates consist of a U-10Mo fuel meat covered with a Zr diffusion barrier layer fabricated by co-rolling, clad in 6061 Al using a hot isostatic press (HIP) bonding process. Specimens exhibited nominal (fresh) fuel meat thickness ranging from 0.25 mm to 0.64 mm, and fuel plate average burnup ranged from approximately 0.36E21 to 6.2E21 fissions/cm^3. After sectioning of the fuel plates, the 6061 Al cladding was removed by dissolution in concentrated NaOH. Pre- and post-dissolution dimensional inspections were conducted on test specimens to facilitate accurate analysis of bend test results. Four-point bend testing was conducted on the Hot Fuel Examination Facility (HFEF) Remote Load Frame at a crosshead speed of 0.1 mm/min using custom-designed test fixtures and calibrated load cells. All specimens exhibited substantially linear elastic behavior and failed in a brittle manner. The influence of burnup on the observed bending modulus and the calculated failure strength is discussed and compared to semi-empirical modulus-porosity relationship models previously proposed in the literature.

3.2 Nomenclature

E *Modulus*

E0 *Fully dense (non-porous) modulus*

b *semi-empirical parameter used in modulus analysis*

p *Porosity*

a – length between points A and B or C and D of the support and load span (note: $a=L/4=S_1/4$)

V – shear force

M – moment force

h – total thickness of specimen

t – thickness of Zr layer

b – width of specimen

y – distance from neutral axis to interface

h_c – thickness of the UMo core

I_h – area moment of inertia for entire specimen

I_{Zr} – area moment of inertia for Zr layers

I_{UMo} – area moment of inertia for UMo core

V_{ll} – load line deflection

E_h – modulus of entire specimen

E_{Zr} – modulus of Zr

E_{UMo} – modulus of UMo

k – curvature

ρ – radius of curvature

ε_x – specimen strain

σxUMo – normal stress in the UMo core

3.3 **Introduction**

Mechanical properties for rolled uranimum 10 wt.% molybdenum (U–10Mo) foils are required to support fuel performance modeling and regulatory qualification of new low enriched uranium monolithic fuel plate designs that incorporate these alloy foils as fuel. Fuel performance modeling and performance testing is done to qualify a low-enriched uranium (LEU) fuel to replace high-enriched uranium (HEU) fuel in research and test reactors for the Office of Materials Management and Minimization (M^3) within the U.S. DOE/National Nuclear Security Administration (NNSA) [1,2,3,4,5]. Measurement of mechanical properties in irradiated fuel is challenging, and limited data exist on the relationships among property, processing, structure, and irradiation conditions of U-10Mo fuel foils relevant to U.S. High Performance Research Reactors (USHPRR). Most available studies reporting properties for U-Mo alloys were conducted in the 1950s and 1960s [6,7,8]. For example, for unirradiated U-Mo alloys, Waldron (1958) [9] reports yield stress, ultimate tensile stress, and modulus for U-Mo alloys with varied weight percentage of Mo in the alloy, heat treatment temperature, and time under heat treatment. More recent work by Burkes [10,11], Ozaltun [12], and Schulthess et al. [13] both summarize existing mechanical property data in the available literature and add to it by exploring variations in fabrication parameters, such as weight percentage Mo, heat treatments, or rolling schedule for rolled DU-10Mo foils.

Gates (1958) [6], reported mechanical property data of irradiated U-Mo alloys. He indicated that the data was obtained from bend tests of specimens with and without cladding. Some of the variables which could affect the data such as fabrication history, heat treatment, burnup, and irradiation temperature were identified. Based on the results, he specified that the mechanical properties of the irradiated reference alloys are affected significantly by two major variables, which are burnup and irradiation temperature. Unfortunately, the range of conditions for which data were evaluated are not particularly relevant to the high burnup and low temperatures of interest for USHPRR applications therefore, no further comparison to this data is made in this work.

Beghi (1968) [7], compiled irradiated properties of U-Mo alloys with different compositions. He included the elastic modulus of irradiated U-10Mo specimens which was originally determined by Leeser (1958) [14]. Similarly, Lotts (1960) [15], compiled properties of irradiated U-Mo and reported effects of irradiation and temperature on the post-irradiation elastic modulus, based on the data reported by Leeser [14]. Like with the data reported in

Gates [6], the data reported by Beghi [7], Lotts [15], and Leeser [14] are for irradiation conditions at higher temperature and lower burnup than the material studied in this work. Therefore, no additional comparison is made.

To support fuel qualification, the selected fuel must demonstrate mechanical and geometric stability. Thus, beyond the fresh fuel mechanical properties, it is of interest to know the evolution or, rather, degradation of the fuel system as a result of irradiation. During irradiation, development of fission-gas bubbles [16,17] and metallurgical reactions [16,17,18,19,20,21,22,23,24] have been reported. For example, previous authors have reported development of interaction layers via diffusion between the U-Mo and Al components of the fuel system. To achieve a high fuel loading, a monolithic fuel system using a Zr diffusion barrier to minimize the adverse metallurgical reaction between fuel and Al-alloy cladding is being developed [25,26,27,28]. Results of previous irradiation testing were reported by Robinson et al. [29], resulting in the down-selection of a fuel design with a baseline fabrication process.

In this study, the degradation of mechanical strength as a result of irradiation is evaluated as a function of porosity. The evolution of microstructure during irradiation is excluded from this study.

To execute the work, it was necessary to develop the required techniques, processes, equipment and methods for mechanical property measurements on irradiated U-10Mo. Limitations imposed by material thickness, available lengths, and current hot-cell fabrication machining abilities mandated use of rectangular specimens tested in bending. The specimen thicknesses of 0.3 to 0.8 mm create undesirably high gradients in principal stress in the material thickness direction, but other constraints allowed no other specimen type or test option. To obtain more representative results, four-point bend loading was performed. Four-point bending results in about half of the specimen length being subjected to constant maximum-bending moment. This resulted in half the surface experiencing maximum bending stress, rather than three-point loading with maximum moment and stress only at the specimen centerline. Test specimens were selected from both the RERTR-12 and AFIP-6 Mk II irradiation campaigns. The RERTR-12 material was irradiated in mini-plate form. The size of the mini-plates is approximately 101 mm by 25.4 mm. The AFIP-6 Mk II material was irradiated in full-size plate form. The size of the full-size plates is approximately 1238 mm by

61 mm. The test specimens had fission densities ranging from 0.4E+21 to 6.3E+21 f/cm^3. The resultant force and deflection data from each specimen were analyzed, and stress at failure and strain at failure were estimated.

3.4 Materials and Methods

3.4.1 Source Materials

The U-Mo monolithic fuel fabrication process for the RERTR-12 and AFIP-6 Mk II irradiation campaigns is described in detail in two INL reports [30,31]. Following casting of the appropriate alloy, the fuel system foil is fabricated by sequential process of hot co-rolling (~650 °C) followed by thickness reductions by cold rolling. The foil is then clad in aluminum by hot-isostatic pressing (at ~520 to 580°C), as illustrated in Figure 3.1 [32]. RERTR-12 and AFIP-6 MKII irradiation experiments were irradiated at the Advanced Test Reactor at the Idaho National Laboratory. Post-irradiation examinations of the RERTR-12 and AFIP-6 MKII irradiation experiments were performed and reported by Rice and Williams [33,34]. Additional details on the source materials and methodologies used for post-irradiation mechanical properties are reported by Lloyd and Schulthess [35].

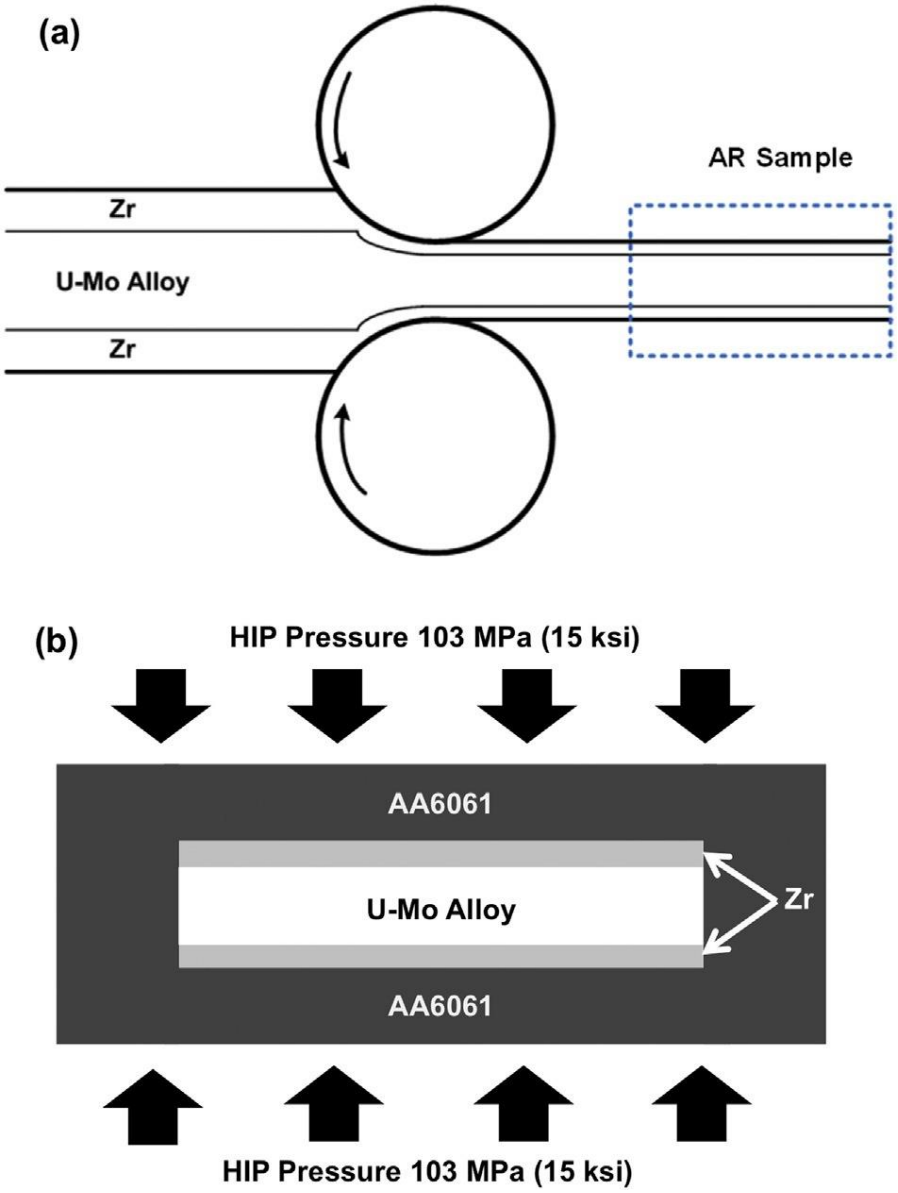

Figure 3.1. Illustration of monolithic plate fabrication (a) co-rolling and (b) hot-isostatic pressing to produce U-10 wt% Mo monolithic fuel encased in AA6061 with Zr diffusion barrier [32].

3.4.2 Test Specimen Preparation

All work with irradiated fuel plates and specimens was completed inside the HFEF Main Hot Cell under a dry argon atmosphere, due to the high radiation levels of the fuel specimens. All operations were performed remotely with master-slave manipulators while viewing the work area through leaded-glass shield windows (see Figure 3.2). Rectangular specimens were cut with a low-speed diamond saw (see Figure 3.3). The test specimens were oriented with specimen length (fixed by the original foil width) oriented parallel to the fuel plate width and specimen width oriented parallel to the fuel plate length, as shown in Figure 3.4. Three bend test specimens were sectioned from each of nine RERTR-12 mini-plates with a target width of 6.0 mm. The three specimens were located adjacent to each other and were centered at approximately 15, 21, and 27 mm from the end of the plate cladding. Six specimens were cut from adjacent locations near the mid-section of the AFIP-6 Mk II test plate in the same relative orientation used for the RERTR-12 sectioning, with a target width of 12.0 mm. An additional three specimens were cut from near the end of the AFIP-6 Mk II fuel zone towards the plate end with the identification marking. Referencing distance from the end of the fuel foil closest to the plate ID label, the specimen centerline positions were at approximately 315, 303, 291, 279, 267, 255, 40, 28, and 16 mm, corresponding to AFIP-6 Mk II specimens A, B, C, D, E, F, G, H, and J. For brevity, no figure of the cut locations of the AFIP-6 MKII test plate is included. Individual specimens were given unique identifications and were tracked throughout the testing.

Two measuring instruments were designed, fabricated, qualified, and calibrated to make the specimen width and thickness measurements. Both instruments use high-precision dial gauges and were modified to work within the constraints of HFEF. As a result, the systematic accuracy is estimated to be ± 20 μm for any individual measurement. The width measurement was performed prior to removal of the aluminum cladding while the thickness measurement was performed after cladding removal. (see Figure 3.5)

The aluminum cladding was dissolved from specimens in a NaOH solution (see Figure 3.6). The initial concentration was 6 M, but became more dilute as the aluminum cladding was dissolved. Periodic additions of more NaOH concentrate were made to the dissolution bath to maintain adequate dissolution rates. The Zr coating on the U-10Mo is not removed in the aluminum dissolution process. The resultant “bare” fuel specimens are actually a composite

structure with the ductile Zr outer layer bonded to the surfaces of the U-10Mo. Owing to the co-rolling fabrication process, the thickness of the Zr layer is known to vary within a range of about 5 to 30 μm, even over small distances within an individual piece of fuel. Effects on test results due to the presence of this variable Zr layer are discussed later. For RERTR-12 specimens, the average Zr thickness was experimentally measured using fresh fuel archives and found to be 24 ±3 μm. For AFIP-6 MkII specimens, the average Zr thickness was experimentally measured also using fresh fuel archives and found to be 20.1 ±2.9 μm

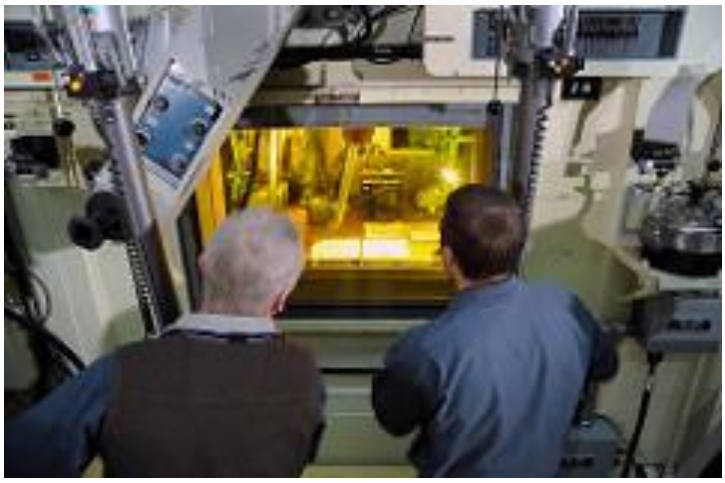

Figure 3.2 Example of HFEF window and performing work using master slave manipulators.

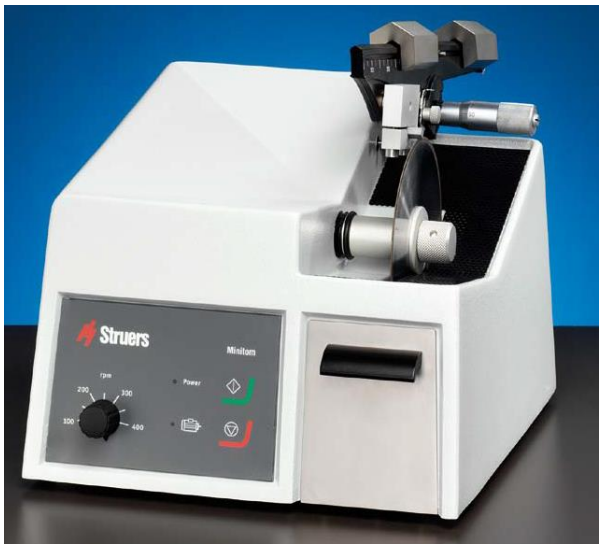

Figure 3.3 Struers Minitom diamond abrasive wafering saw like the one used for plate sectioning.

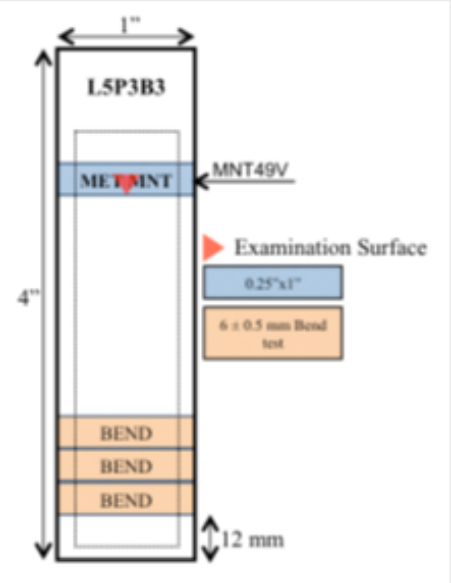

Figure 3.4. Diagram showing specimen sectioning orientation and locations in RERTR-12 test fuel plates.

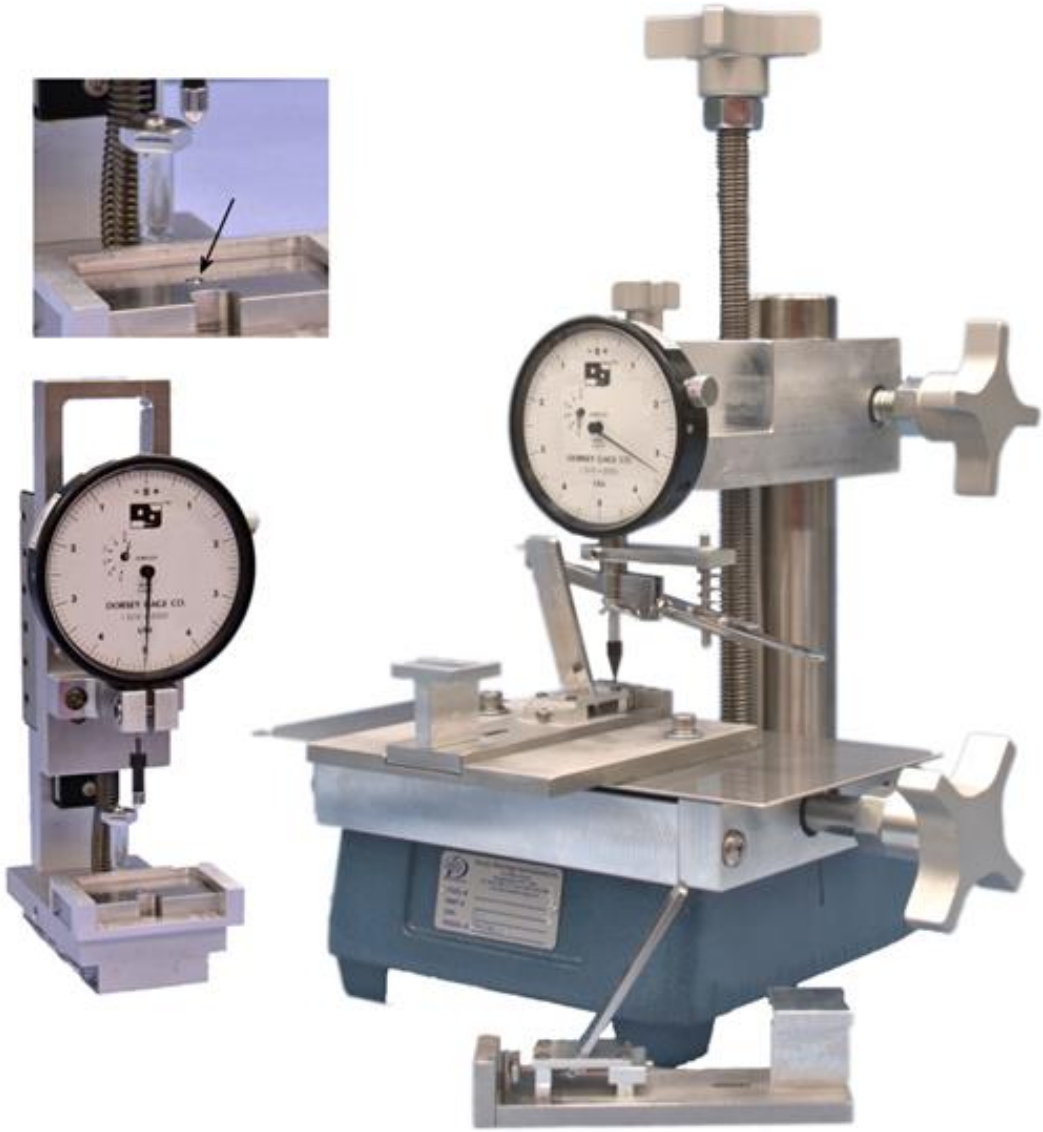

Figure 3.5 Test specimen thickness (left) and width (right) measuring instruments. The dial gauges are about 80 mm in diameter. Specimen holder for width measurement of RERTR-12 specimens is installed on the width measuring stand; the holder for the wider AFIP-5 Mk II specimens is shown in from of the stand.

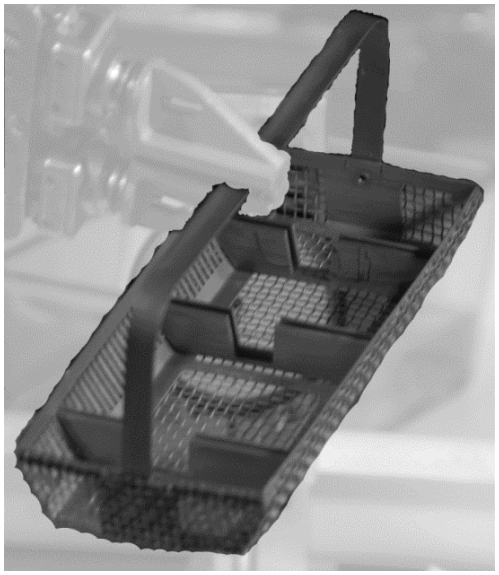

Figure 3.6 Cladding dissolution tray.

3.4.3 Mechanical Testing

A highly customized Instron 5869 electromechanical test machine was designed, built, and installed in the HFEF Main Cell. All control, signal-conditioning, and motor-power components were separated from the test frame and located outside of the hot cell. A sealed and shielded electrical feed-through connects the outside components to the test frame electrical components. All of the frame wiring and electromechanical components use radiation-resistant insulation and materials. The drive motor brushes are a special material ("high altitude" brushes) that provides greatly improved service life in the dry argon environment.

A high-resolution analog resolver is attached to the drive-motor output shaft and provides feedback for crosshead position. The data acquisition and processing of the resolver signal yields a crosshead displacement resolution of better than 0.05 µm, but the double-reduction toothed belt-drive system attached to ball-nut lead screws that move the machine crosshead suggest the relative accuracy of actual crosshead motion over a few millimeters of travel is probably larger. Subsequent testing using an independent deflectometer identified the error to be on the order of a few-tenths of microns.

Normal strain-gauge-type load cells constructed with radiation-resistant wiring provide force feedback signals. Different load cells with quick-connect attachments provide a wide range of accurate force measurements. The lowest-capacity load cell has a 50 N full-scale capacity and was used for all AFIP-6 Mk II specimens and some of the RERTR-12 specimens. The remaining specimens were tested using a 500 N-capacity load cell. The compliance of each load cell is known and was used to calculate load point displacements that are more accurate than the direct crosshead position information.

The bend test fixtures were designed to meet various requirements of use in the hot cell for testing very thin specimens, and both fixtures use the same design, and have a nominal 2:1 load-to-support span ratio (S1 or L = support span, S2 = load span). The actual spans for RERTR-12 fixture are S1 = 16.02 and S2 = 7.95 mm (ratio 2.02); AFIP-6 Mk II fixure spans are S1 = 29.96 and S2 = 15.04 mm (ratio 1.99). The RERTR-12 bend test fixture is shown in Figure 3.7. The AFIP-6 Mk II test fixture is equivalent with support and load spans as provided above.

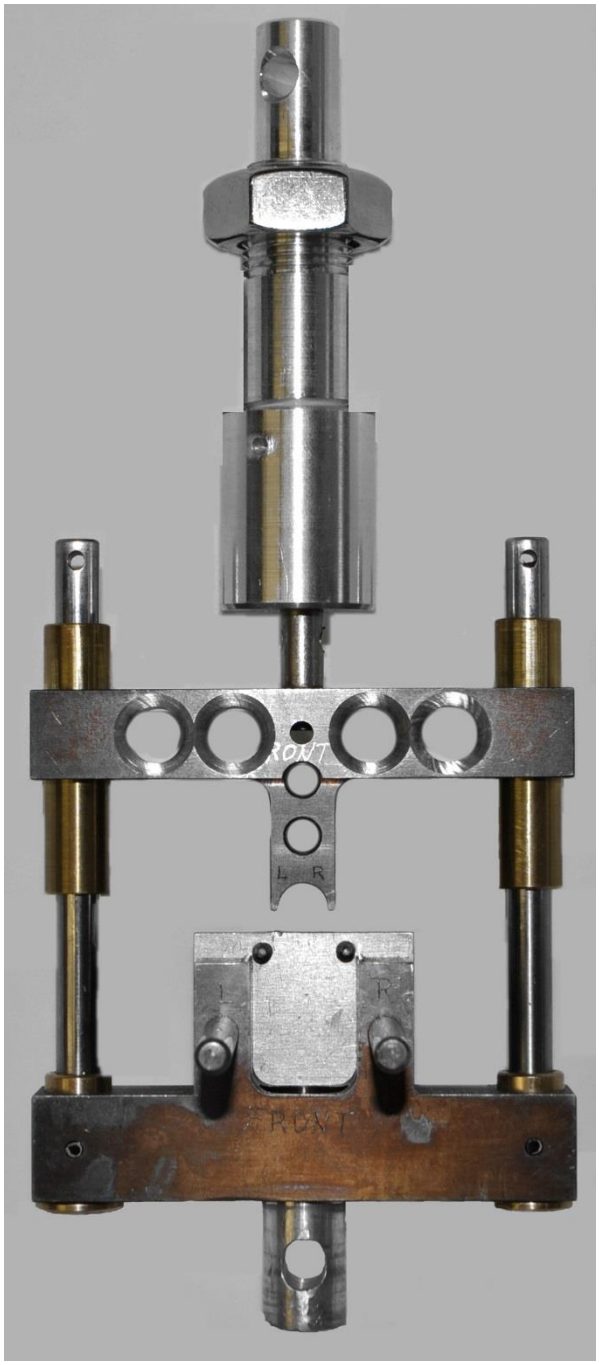

Figure 3.7. Bend test fixture used for RERTR-12 specimen tests. Top and bottom round clevis attachments are 12 mm dia.

3.5 Theory/Calculation

3.5.1 Data Analysis and Corrections

The raw data files generated by the test system during a test require various processing prior to final analysis to determine specimen properties.

The compliance of the load cells used for these tests was the dominant source of error between the resolver-indicated machine crosshead displacement and the actual load point contact displacement at the specimen. Each load cell compliance value was measured prior to its placement into the hot cell. The appropriate compliance value was used for each data set to convert the “machine crosshead displacement” into the specimen load point displacement. These corrected displacements are used in subsequent calculations of estimated specimen bending strains.

The custom Instron 5869 test system at the HFEF hot cell had an issue with electrical noise, generated by the drive-motor wiring, creating anomalous force readings when the drive motor ran at the time this testing was conducted. There was an initial offset in the force reading when the motor power was applied, and the offset magnitude was not consistent. Simultaneously, a somewhat cyclic noise signal with a fundamental period of about 1 sec was superimposed while the motor continued to run. The character of the cyclic noise signal was not sufficiently uniform to remove it from the data. However, the peak-valley amplitude of the noise signal is reasonably constant at about 0.15% of load cell full-scale capacity. With this knowledge, we elected to use the local peak force values in each noise cycle to be representative of the specimen response during that cycle. This approach yields well over 100 data points for each specimen test, providing a well-behaved force-deflection response curve.

The self-aligning bend fixture design causes a force plateau early in each test as the clearance (~0.08 mm) in the self-aligning slip joint is closed by machine crosshead movement. The force applied to the specimen during this plateau is equivalent to the fixture crosshead weight below the slip joint, 0.7 N for both fixtures. The specimen has no additional deflection during this plateau, so the plateau portion of data is removed, and subsequent deflection data are offset to align with the pre-plateau data, resulting in a smooth load-deflection curve. Due to the force offset occurring when motor power is applied, a reliable

force zero cannot be set prior to the start of a test. The indicated force levels at the force plateau and after specimen failure (while the motor was running) were evaluated, and the force data were offset as necessary to match the known force values. This results in a force at specimen failure accuracy of about 0.1 N.

The noise issue identified during this testing has subsequently been corrected via the installation of a new feedthrough in the HFEF shield wall.

3.5.2 Bending Strain, Stress, and Modulus Estimation for the Composite Specimen with a Known Zr Thickness

The bending strain, stress and modulus for the composite test specimen can be estimated from the corrected load point-deflection data discussed previously. Some assumptions are required in order to derive the necessary functions. The assumptions include elastic specimen response and small geometry change in the specimen. The corrected force and deflection response curves generally have a significant linear section, sometimes completely up to the point of failure. This is a good indication of bulk elastic response of the test specimen. The small geometry change is validated by looking at the ratio of support span to specimen thickness and support span to maximum specimen deflection. The ratios are both greater than 20 for every test, and the resultant calculated surface strains at failure are all less than 1%. These observations validate the required assumptions to derive the elastic, small-geometry-change deflection-to-strain function.

The derivation is based on the second order moment curvature equation found in all Mechanics of Materials texts [36]. For this evaluation, the ‘direct method’ Bernoulli-Euler beam theory for a bi-metallic beam is used and provides a closed-form solution to extract the strain, stress, and modulus of the U-10Mo fuel from the composite structure tested. Variables used are defined in the following paragraphs and, where relevant, shown in the following figures. A free-body diagram is shown in Figure 3.8 and is used to solve for the constant bending moment in the center section (region of interest) of the beam. The center of the beam is in pure bending; thus, no shear forces are present. Variables are defined as follows:

P –applied load

L or S1 – bend fixture support span length

S2 – bend fixture load span (note: S1/S2 ~ 2)

a – length between points A and B or C and D of the support and load span (note: $a=L/4=S_1/4$)

V – shear force

M – moment force

h – total thickness of specimen

t – thickness of Zr layer

b – width of specimen

y – distance from neutral axis to interface

h_c – thickness of the UMo core

I_h – area moment of inertia for entire specimen

I_{Zr} – area moment of inertia for Zr layers

I_{UMo} – area moment of inertia for UMo core

V_{ll} – load line deflection

E_h – modulus of entire specimen

E_{Zr} – modulus of Zr

E_{UMo} – modulus of UMo

k – curvature

ρ – radius of curvature

ε_x – specimen strain

σ_{xUMo} – normal stress in the UMo core

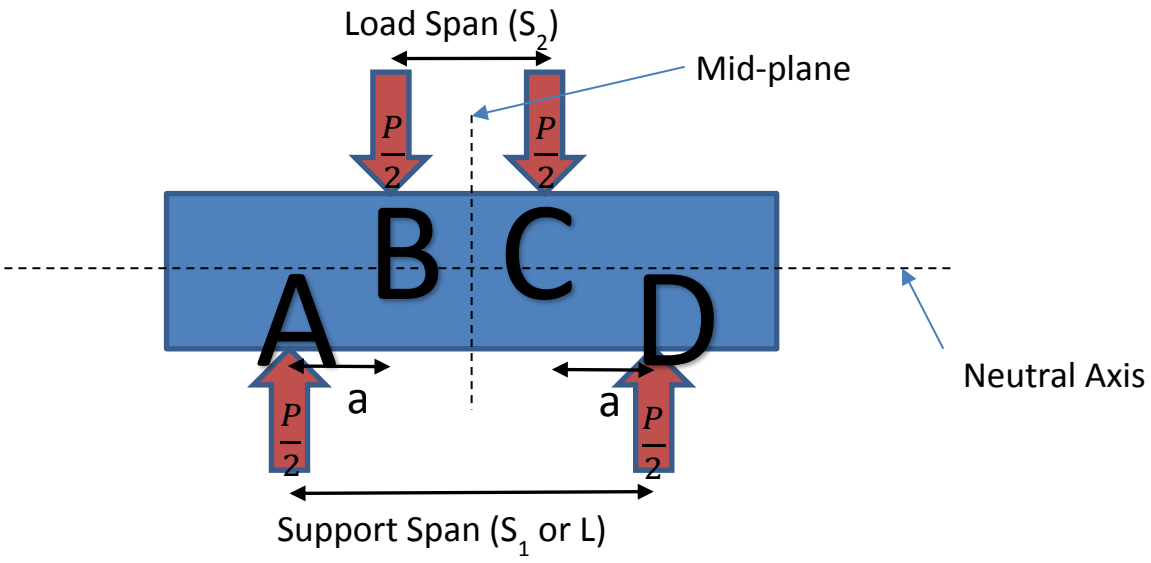

Figure 3.8. Free body diagram of four-point bend test.

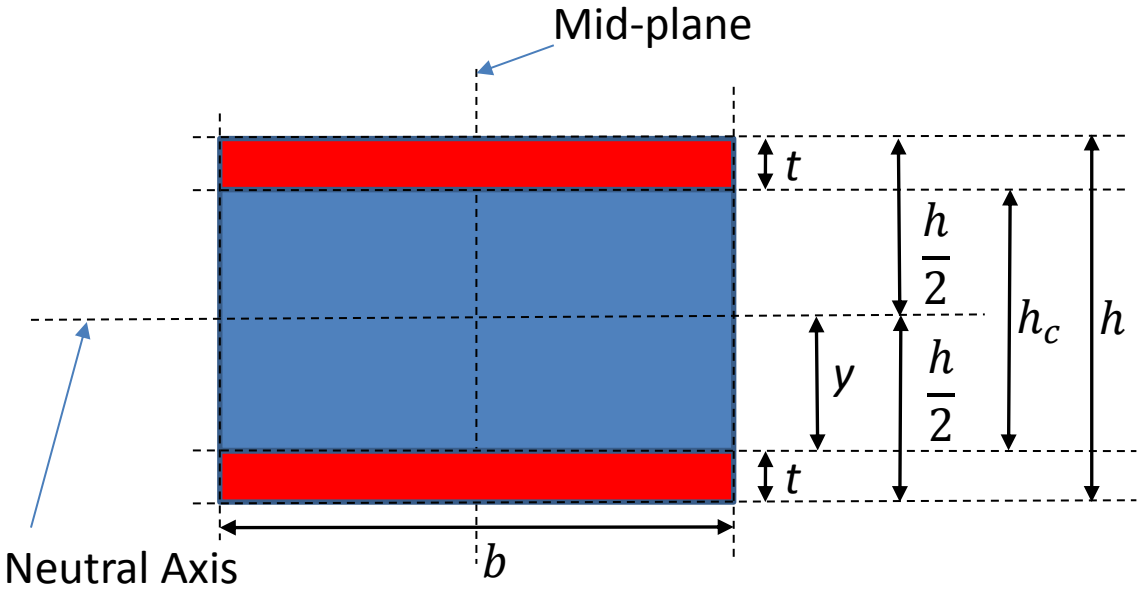

Figure 3.9. Schematic of composite specimen showing variable definitions for specimen geometry used in equations.

$$\mathrm{M}(x) = \frac{PL}{8} \tag{1}$$

Based on the definition of variables shown in Figure 3.9, the following equations based on specimen geometry are provided: see equations (2), (3), (4), (5), (6). In the subsequent analysis, *h* is the experimentally measured overall or total thickness of each specimen. The Zr thickness or *t* is also measured experimentally on as-fabricated fresh-fuel archives. For RERTR-12 specimens, the average Zr thickness was experimentally measured to be 24 ±3 μm [37]. For AFIP-6 MkII specimens, the average Zr thickness was experimentally measured to be 20.1 ±2.9 μm [38].

$$\mathrm{y} = \frac{(\mathrm{h} - 2\mathrm{t})}{2} \tag{2}$$

$$h_c = h - 2t \tag{3}$$

$$I_h = \frac{bh^3}{12} \tag{4}$$

$$I_{Zr} = \frac{b(h^3 - h_c^3)}{12} \tag{5}$$

$$I_{UMo} = \frac{bh_c^3}{12} \tag{6}$$

Now by using the displacement equation for four-point bending, equation (7), the deflection curvature relationship, equation (8), and the strain curvature relationship, equation (9), we can find the strain in the specimen at any location y from the neutral axis as only a function of geometry and deflection—equation (10).

$$v_{ll} = \frac{Px}{6E_h I_h}(3aL - 3a^2 - x^2) \; for \; 0 \le x \le a \tag{7}$$

$$k = \frac{1}{\rho} = v_{ll}'' \tag{8}$$

$$\varepsilon_x = \frac{-y}{\rho} = -ky \tag{9}$$

$$\varepsilon_x = \frac{-12yv_{ll}}{L^2} \tag{10}$$

Then by using the moment curvature relationship, shown in equation (11), we can rearrange and find the modulus of the U-Mo core, equation (12), by assuming a value of the modulus of Zr and utilizing the curvature from equation (8). In this case, the modulus of Zr was chosen to be 87.2 GPa. This modulus was chosen to be consistent with the AFIP-7 bend test analysis documented in ECAR-4051 [39,40,41,42,43]. Finally, we can find the normal stress in the UMo component of the composite beam by using equation (13).

$$k = \frac{1}{\rho} = \frac{M}{(E_{Zr}I_{Zr} + E_{UMo}I_{UMo})} \tag{11}$$

$$E_{UMo} = \frac{M - kE_{Zr}I_{Zr}}{kI_{UMo}} \tag{12}$$

$$\sigma_{xUMo} = \frac{-MyE_{UMo}}{E_{Zr}I_{Zr} + E_{UMo}I_{UMo}} \tag{13}$$

3.5.3 Specimen Fission Density Estimation

Fission density (f/cm³) depends on many factors and is estimated by numerical simulations using a qualified physics model and known irradiation conditions in the reactor. Neutronics simulations typically produce matrices of fission-density values corresponding to location increments throughout the material. As-run neutronics simulations were performed for both the RERTR-12 and AFIP-6 Mk II irradiation campaigns. The fission densities used in this document are taken from these neutronics simulations, which are reported elsewhere [44,45]. It is noted that the original neutronics simulations and fission densities were revised between 2012 and 2016. This work uses the revised fission density values.

3.5.4 Specimen Porosity Estimation

While it is known that porosity driven by fission-gas bubbles in the U-Mo fuel increases with increasing fission density during irradiation [46,47,48] there is very limited data where porosity is quantified as a function of fission density. At present, the available data are from [46], which performs image analysis to obtain a porosity value of images from KGT-1225, a sample of U-7Mo dispersion fuel with magnesium matrix from the RERTR-8 irradiation experiment. Because the present work is performed on U-10Mo, the porosity values from [46] are not applicable to this analysis.

Some relevant porosity data on irradiated monolithic U-10Mo material, compared to fission density, are available in a report from Robinson [49]. These porosity data are considered preliminary due to the difficulty of preparing samples of adequate quality for image analysis. It was beyond the scope of this work to obtain quantified values of porosity of irradiated U-10Mo samples; therefore, the available data are used. While these data are used in this analysis, it is recommended that this analysis be revisited when additional porosity data become available. Nevertheless, the porosity values obtained were from samples taken adjacent to the samples used in the bend test, therefore, differences in the irradiation temperature, or burnup between the metallographic samples used for porosity estimation and the samples used for bend testing is considered negligible.

3.5.5 Degraded Modulus Analysis

Notable work has been performed documenting the relationship of mechanical properties of heterogeneous materials such as those with identifiable porosity. Some of the earliest of these were by Einstein [50] where the viscosity of a suspension was determined, assuming that it may be described by rigid spherical particles, suspended in a viscous fluid, and that the volume concentration of the spheres is so small that they do not interact [51]. The following analysis is focused on the degradation of modulus. A similar analysis could be performed for degradation of ultimate strength.

Eudier [52] in 1962, suggested a 2/3 power model, which was further refined by Hyun [53] in 2001, where spherical pores are arranged in a simple cubic pattern. Their equation is remarkably similar to that described and used by Martin [54,55] in 1971 and takes the form [56]:

$$E = E_0(1 - bp^{2/3}) \tag{14}$$

where E_0 is the fully dense (non-porous) Young's modulus, E is the degraded modulus based on increasing porosity, p is the porosity, and b is a constant that varies with pore geometry and material.

Fryxell [57] in 1964 used a linear degradation model which takes the form [56]:

$$E = E_0(1 - bp) \tag{15}$$

where E_0 is the fully dense (non-porous) Young's modulus, E is the degraded modulus based on increasing porosity, p is the porosity, and b is a constant that varies with pore geometry and material.

Rice [58] in 1993, evaluated several models including an exponential relationship model first used by Spriggs [59] in 1961 and concluded that models for the porosity induced degradation based on minimum solidus area outperformed those based on stress concentrations from porosity such that:

$$E = E_0 e^{-bp} \tag{16}$$

where E_0 is the fully dense (non-porous) Young's modulus, E is the degraded modulus based on increasing porosity, p is the porosity, and b is related to the particle stacking and pore shape [60,61,62,63]. For some materials, such as those evaluated by Knudson [61], b has been determined empirically. Based on the work of Knudson, b may be on the order of 4.

Alternatively, Ramakrishnan and Arunachalam [64], in 1990, proposed a model based on continuum mechanics and utilizing the increasing porosity along with the Poisson's ratio of the fully dense material. The form of this equation was first proposed by Hasselman [65] in 1962 and was based on the work of Hashin [51]. In the earlier works, the numerator is not

squared [56]. For this work, the authors chose to use the form, including the squared numerator, as proposed by Ramakrishnan and Arunachalam [64]:

$$E = E_0 \frac{(1-p)^2}{(1+pb_\theta)} \tag{17}$$

where E_0 is the fully dense (non-porous) Young's modulus, E is the degraded modulus based on increasing porosity, p is the porosity, and b_θ is a constant that is between 2 to 3 times the Poisson's ratio of the fully dense material.

Using fully dense modulus values from Schulthess [13], and the porosity values from Robinson [49], degraded modulus values are estimated using each of the proposed models and compared to the experimentally determined values.

3.6 **Results**

Graphical representations in the following figures show the experimentally determined ultimate strength and modulus values of both fully dense unirradiated U-10Mo and irradiated U-10Mo with porosity induced from irradiation. The analysis focused on the degradation model for the modulus, so Figure 3.10 includes data points that estimate modulus based on the models previously discussed. Figure 3.11 shows the ultimate strength values but does not include degradation model analysis although such analysis would be similar to that performed for modulus.

The fully dense unirradiated strength and modulus values were obtained from the work discussed in Chapter 2. This work was performed on bare material (i.e. no Zr layer), and by uni-axial tensile testing methodology. While these values are included, and comparison is made to the results of the composite irradiated material interrogated by four-point bend testing, some caution is warranted when comparing the results. The tensile tests result in the entire material cross section being subjected to a uniform tensile force, while in the bend test, the constant bending moment between the points of the loading span result in a gradient of compressive force on the half of the specimen thickness above the neutral axis, and a gradient of tensile force on the half of the specimen thickness below the neutral axis. In this case, only the outer most finite element is subjected to the maximum tensile force.

Separate from this work, Lloyd et al. [35] developed an FEA model, using ABAQUS, of the four-point bend test for select specimens from the RERTR-12 source material that was used in this work. Reasonable agreement between the results from the composite plate theory used in this work, and the FEA model developed by Lloyd were found. However, the results of the two separate analysis do not exactly match. Sources of uncertainty discussed in this paper likely contribute to the discrepancies in the values such as the large variation found between replicate specimens simply due to the nature of brittle failure statistics. An added discrepancy is that the FEA model accounts for friction in the results while the composite beam theory does not. Further, in the FEA case, the bending is idealized with the specimen in full contact with the loading and support spans, which may not account for any specimen geometry variations or twisting/warping as is the case for the experimental test.

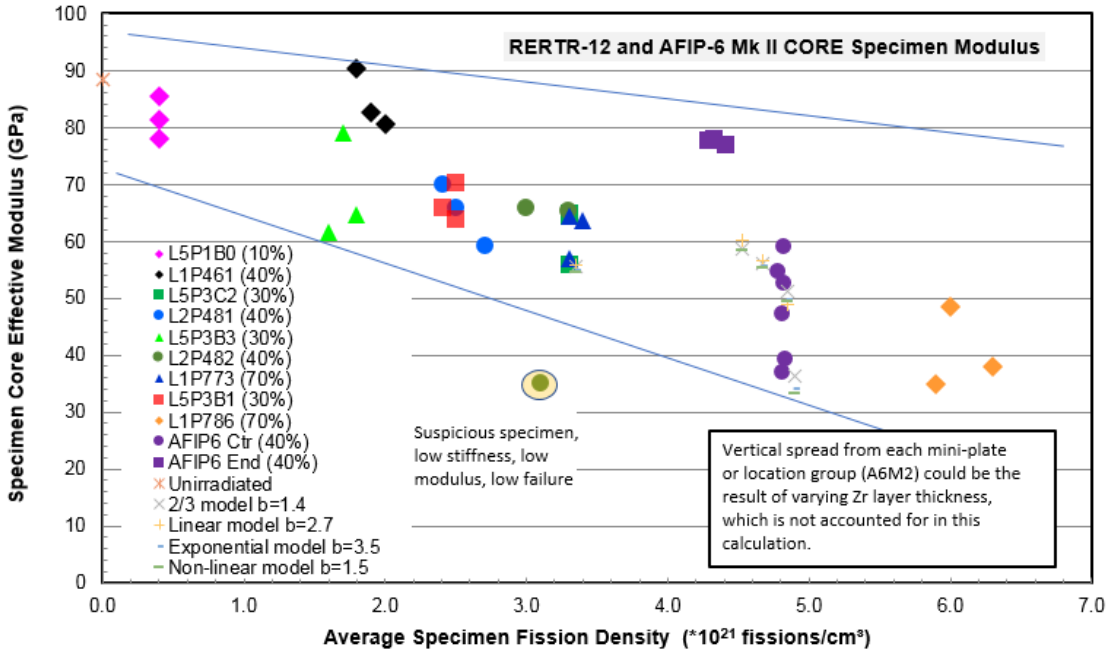

Figure 3.10. Experimental Modulus values for unirradiated and irradiated U-10Mo. Also shows values for four different models based on porosity to match the degradation of the modulus.

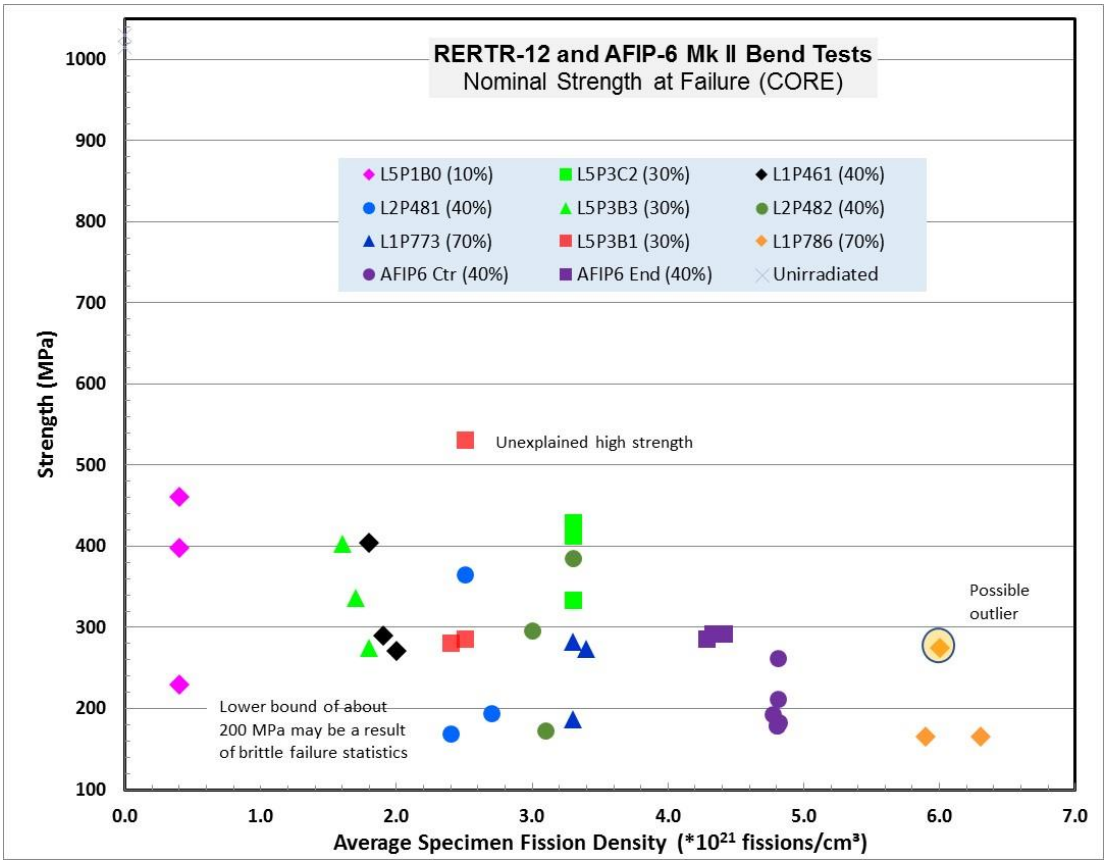

Figure 3.11. Experimental strength values for unirradiated and irradiated U-10Mo. Note the significant decrease in strength at very low fission density values.

3.7 Discussion

3.7.1 Ductility and Strength Loss in Irradiated Material

Room-temperature tensile properties of unirradiated U-10Mo foil that has been cold worked to 50% reduction and subsequently annealed has ultimate strength values of 1015 MPa and 1030 MPa, depending on the orientation of the test specimen relative to the rolling direction. These room-temperature tests also exhibited ductile elongation from 1.24% to 1.35% [13]. By contrast, the irradiated foil material in this work, which was processed under similar thermo-mechanical rolling conditions prior to irradiation, exhibited essentially elastic behavior up to the point of fracture, and failure occurred in a brittle manner resulting in a kind of fracture strength rather than yield strength. There was no measurable specimen ductility in these specimens. Most significantly, the highest recorded strength for the U-Mo core for any irradiated specimen tested was 531 MPa, indicating substantially reduced fracture strength that is dominated by major flaws in the structure of the material compared to unirradiated material.

3.7.2 Bending Failure Strength and Fission Density Correlation

Figure 3.11 shows an expected degradation of the strength of the U-Mo material as fission density increases. Ignoring, for a moment, specimens that are likely outliers, the specimens with the lowest fission density, those from plate L5P1B0 with 0.4E+21 f/cm^3, had the highest bend strength values in the range of 420 MPa. The specimens with the highest fission density, those from plate L1P786 with 5.9E+21 f/cm^3 to 6.3E+21 f/cm^3, had the lowest strength values in the range of 165 MPa.

Two specimens had suspiciously high bend strength. L1P786-21 had bend strength of the U-Mo core of 274 MPa at 6.0E+21 f/cm3. L5P3B1-15 had bend strength of the U-Mo core of 531 MPa at 2.5E+21 f/cm^3. Conversely, specimen L5P1B0-15 had low bend strength of the U-Mo core at 229 MPa at 0.4E+21 f/cm^3 compared to the other specimens in the set. The data and testing procedures for these apparent outliers was reviewed and nothing unusual was revealed that would have contributed to such results. Significant variability is noted in the results as is apparent by looking at Figure 3.11, but all values except for the noted outliers fall within the general trend of the entire data set. Variabilities between specimen groups with similar fission densities such as between L5P3C2 and L1P773, where the

specimen groups are clearly separated, indicate a systematic difference not related to testing procedure or data analysis. Such a variation may be a result of microstructural difference caused by fabrication variables, or differences in burnup profile from different irradiation conditions such as power and temperature. A comparison with metallographic data generated during post-irradiation examination may also suggest if significant differences in irradiated microstructure were present in the tested specimens.

3.7.3 Elastic Modulus and Fission Density Correlation

The elastic modulus of the U-10Mo material is expected to decrease with increasing fission density due to gas bubble formation in the material. This is expected to be the dominant factor in reduction of elastic modulus as burn-up increases. Figure 3.10 shows that the modulus degraded with increasing fission density as expected. Less variability existed in this data set compared to the variability in the strength values. Nonetheless, one specimen had suspiciously low stiffness and low modulus of the UMo core. L2P482-21 had a modulus of 35 GPa at 3.1E+21 f/cm3. The other specimens in this group had modulus values in the range of 65 GPa at similar fission density. The data and testing procedure for this outlier was review and nothing unusual was revealed that would have contributed to such results.

Similar to the observation in the strength, variabilities exist between specimen groups with similar fission densities. For the modulus, these group variabilities are noted between L1P461 and L5P3B3 at ~1.8E+21 f/cm3, and also between the AFIP-6 MkII end specimens and the AFIP-6 MkII center specimens at 4.3E+21 f/cm3 and 4.8E+21 f/cm3 respectively. As previously discussed, additional investigation into differences in microstructural or irradiation conditions may reveal cause for such variation. For example, the the AFIP-6 MkII plate was a full size plate and it is possible a temperature difference existed during irradiation between the center and the end of the plate.

3.7.4 Sources of Data Variability

There are a number of possible sources for the observed variability in the calculated results. Differences in source materials, enrichments, fabrication process variables, microstructure, and irradiation conditions may have multi-variate effects that are not presently accounted for.

Reported bend strengths use a weighted average specimen thickness and width in order to apply closed form stress calculations, and all the specimens had some variations in thickness and width. The thickness variable has an inverse cubed relationship to calculated stress, the specimens are very thin, and the thickness variations can be a significant percentage of the average thickness. The calculated stresses reported are at the outer surface of the specimen. A first order estimate of surface bend stress range for each specimen could be bounded using maximum and minimum measured thickness and widths.

Reported surface bend strains also use the weighted average thickness, and the strain is a linear function of specimen thickness. The weighted average irradiated specimen thicknesses ranged from 310 to 829 μm. Individual specimen thickness variations were typically no more than 30 μm, but a few specimens had variations exceeding 90 μm. Most of this variation is expected to be the result of non-uniform radiation-induced swelling of the U-10Mo which can be significant at higher fission densities. The calculated strain error could be rather small to quite significant relative to flexural stiffness depending on the thickness distribution and magnitude relative the weighted average for that specimen.

Nominal specimen force-deflection response was linear to the point of failure for each test, indicating bulk elastic material response and no measurable ductility. The failure mode of the irradiated U-10Mo tested is therefore brittle, and likely has very low fracture resistance. Any material with these general characteristics have wider variations in measured strength due to significant effects of small defects, possibly undetectable, in the material. These effects are exacerbated by the small volume of stressed material in these specimens and presently unknown distribution of defect sizes and corresponding spatial defect distributions in the material. Such information, if available, can be used to determine a material strength distribution as a function of stressed volume.

The pure Zr coating on the U-10Mo surfaces is affected little by the irradiation. However, the analysis used to extract the properties of the U-Mo fuel core assumed a constant thickness of Zr and did not account for localized Zr thickness variations that are known to vary over sub-millimeter distances from less than 5 to over 30 μm. In an effort to bound this effect, the average Zr thickness $\pm 1\ \sigma$ was evaluated for both the RERTR-12 and AFIP-6 MkII specimens. For the RERTR-12 specimens, this impact was small at less than 1%. For the AFIP-6 MkII specimens however, the impact was more significant at -3.5% to +4.5%. The

exact properties of the Zr layer as a result of fabrication conditions and irradiation are not documented; therefore, the analysis used assumed values for properties. Any differences between as irradiated Zr properties and those assumed may further influence the results.

In a few cases, some very small load drops prior to final specimen failure were observed. It is possible that the ductile Zr coating was thick enough that a micro-crack initiation was arrested after small extension through energy absorption by plastic deformation of the bonded Zr coating. Continuing specimen deflection supplied more energy, resulting in more crack advancement at later times in the test. At some point, the Zr ultimate strength would be locally exceeded, and the absorbed energy would return to the growing crack, leading to catastrophic failure of the specimen.

3.7.5 Comparison of Porosity Degradation Models to Experimental Data

The experimental data were compared to the data from the four different semi-empirical models discussed previously. Due to uncertainty in the porosity data that were used as an input to the models, and the limited range of fission densities available for the porosity data, a comparison over only a narrow range of fission densities was possible. However, by comparing relative slopes over this narrow range, it may be possible to extend the model to the full set of data. Therefore, a linear regression was performed for the entire set of experimental data, including the unirradiated values. The slope and intercept of this linear regression was compared to the slope and intercept of four individual linear regressions of the data produced by the four semi-empirical models. This comparison identified that the slope and intercept of the non-linear model, equation (17), is the closest match. As a result, the degradation of the modulus with increasing fission density can be accurately described by the non-linear model, equation (17), and can be attributed, in large part, to the porosity increasing with fission density. Despite this result, due to the large uncertainty previously discussed, it is strongly recommended that this evaluation be revisited when additional irradiated U-10Mo mechanical properties and porosity data become available.

3.8 References

1 J.L. Snelgrove, G.L. Hofman, M.K. Meyer, C.L. Trybus, T.C. Wiencek, “Development of very-high-density low-enriched-uranium fuels,” *Nucl. Eng. Des.* 178 (1997) 119-126).

2 J. F. Jue, B.H. Park, C.R. Clark, G.A. Moore, D.D. Keiser Jr., “Fabrication of monolithic RERTR fuels by hot isostatic pressing,” *Nucl. Technol.* 172 (2010) 204-210.

3 D. D. Keiser Jr., S.L. Hayes, M.K. Meyer, C.R. Clark, “High-density, low-enriched uranium fuel for nuclear research reactors,” *JOM* 55 (2003) 55-58.

4 D. M. Wachs, *RERTR Fuel Development and Qualification Plan*, INL/EXT-05-01017 Idaho National Laboratory, Idaho, USA, 2007.

5 S. Van Den Berghe, A. Leenaers, E. Koonen, L. Sannen, “From high to low enriched uranium fuel in research reactors,” *Adv. Sci. Technol.* 73 (2010) 78-90.

6 J. E. Gates, E.G. Bodine, J.C. Bell, A.A. Bauer, G.D. Calkins, *Stress-Strain Properties of Irradiated Uranium-10 w/o Molybdenum*, BMI-APDA-638, Battelle Memorial Institute, Columbus, OH, January, 1958.

7 G. Beghi, *Gamma Phase Uranium-Molybdenum Fuel Alloys*, EUR-4053e, European Atomic Energy Community, 1968.

8 K. G. Hoge, “Some mechanical properties of U-10% Mo alloy under dynamic tension loads,” *J. Basic Eng.* 6 (1966) 509-517.

9 M.B. Waldron, R.C. Burnett, S.F. Pugh, *The Mechanical Properties of Uranium–Molybdenum Alloys*, UK Atomic Energy Authority Technical Report, ARE-MB-2554, 1958.

10 D.E. Burkes, R. Prabhakaran, J.F. Jue, F. Rice, “Mechanical Properties of DU-xMo Alloys with x = 7 to 12 Weight Percent,” *Metall. and Materials Trans. A* 40A (2009), 1069-1079.

11 D.E. Burkes, R. Prabhakaran, T. Hartmann, J.F. Jue, F.J. Rice, “Properties of DU-10 wt% Mo alloys subjected to various post-rolling heat treatments,” *Nucl. End. Des.* 240 (2010) 1332-1339.

12 H. Ozaltun, M-H., Herman Shen, and P. Medvedev, “Assessment of residual stresses on U10Mo alloy based monolithic mini-plates during Hot Isostatic Pressing,” *J. Nucl. Mater.* 419.1 (2011), 76–84.

13 J. Schulthess, R. Lloyd, B. Rabin, M. Heighes, T. Trowbridge, E. Perez, “Elevated Temperature Tensile Tests on DU-10Mo Rolled Foils,” *J. Nucl. Mater.*, 510 (2018) 282-296.

14 D.O. Leeser, F.A. Rough, and A.A. Bauer, “Radiation Stability of fuel elements for the Enrico Fermi Power Reactor,” *Int. Geneva Conference 1958 – Paper P/622.*

15 A.L. Lotts, *Review of information on U-Mo alloys and U-Mo-UO2 dispersion fuels,* ORNL 60-6-122, No:50, Oak Ridge National Laboratory, 1960.

16 Y.S. Kim, G. L. Hofman. “Fission product induced swelling of U–Mo alloy fuel.” *J. Nucl. Mater.* 419.1 (2011): 291-301.

17 Y.S. Kim, G.L. Hofman, J.S. Cheon, A.B. Robinson, D.M. Wachs. “Fission induced swelling and creep of U–Mo alloy fuel.” *J. Nucl. Mater.* 437.1 (2013): 37-46.

18 M.K. Meyer, G.L. Hofman, S.L. Hayes, C.R. Clark, T.C. Wiencek, J.L. Snelgrove, R.V. Strain, K.-H Kim. “Low-temperature irradiation behavior of uranium-molybdenum alloy dispersion fuel,” *J. Nucl. Mater.* 304 (2002) 221-236.

19 H. Palancher, P. Martin, V. Nassif, R. Rucoulou, O. Proux, J.-L. Hazemann, O. Tougait, E. Lahera, F. Mazaudier, C. Valot, S. Dubois., “Evidence for the presence of U-Mo-Al ternary compounds in the U-Mo/Al interaction layer grown by thermal annealing: a coupled micro X-ray diffraction and micro X-ray absorption spectroscopy study,” *J. Appl. Crystallogr,* 40 (2007) 1064-1075.

20 H. Ryu, J. M. Park, C.K. Kim, Y.S. Kim, G.L. Hofman., “Diffusion reaction behaviors of U-Mo/Al dispersion fuel,” *J. Phase Equilib. Diffus.* 27 (2006) 651-658.

21 F. Mazaudier, C. Proye, F. Hodaj., “Further insight into mechanisms of solid state interactions in UMo/Al system”, *J. Nucl. Mater.* 377 (2008) 476-485.

22 E. Perez, D.D. Keiser Jr., Y.H. Sohn., “Phase constituents and microstructure of interaction layer formed in U-Mo alloys vs Al diffusion couple annealed at 600 °C,” Metall. Mater. Trans. A 42 (2011) 3071-3083.

23 B. Yao, E. Perez, D.D. Keiser Jr., J.F. Jue, C.R. Clark, N. Woolstenhulme, Y. Sohn., “Microstructure characterization of as-fabricated and 475 °C annealed U-7 wt.%Mo dispersion fuel in Al-Si alloy matrix,” *J. Alloys Compd.* 509 (2011) 9487-9496.

24 D. D. Keiser Jr., J.F. Jue, B. Yao, E. Perez, Y. Sohn, C.R. Clark., “Microstructural characterization of U-7Mo/Al-Si alloy matrix dispersion fuel plates fabricated at 500 °C,” *J. Nucl. Mater.* 412 (2011) 90-99.

25 E. Perez, B. Yao, D.D. Keiser Jr., Y.H. Sohn., “Microstructural analysis of as-processed U-10 wt.%Mo monolithic fuel plate in AA6061 matrix with Zr diffusion barrier,” *J. Nucl. Mater.* 402 (2010) 8-14.

26 G. A. Moore, M.C. Marshall., *Co-rolled U10Mo/Zirconium-barrier Layer Monolithic Fuel Foil Fabrication*, INL/EXT-10-17774 Idaho National Laboratory, Idaho, USA, 2010.

27 G.A. Moore, F.J. Rice, N.E. Woolstenhulme, W.D. Swank, D.C. Haggard, J.F. Jue, B.H. Park, S.E. Steffler, N.P. Hallinan, M.D. Chapple, D.E. Burkes., *Monolithic Fuel*

Fabrication Process Development at the Idaho National Laboratory, INL/Con-09-17298, Idaho National Laboratory, Idaho, USA, 2009.

28 K.H. Kim, S.J. Oh, D.B. Lee, C.K. Kim, D.S. Sohn., "Continuous casting of wide U-7wt.%Mo alloy foils for a monolithic fuel by a single cooling roll," *Transactions of the 10th International Topical Meeting on Research Reactor Fuel Management*, European Nuclear Society, Sofia, Bulgaria, 2006, pp. 83-86.

29 A. B. Robinson, G.S. Chang, D.D. Keiser, Jr., D.M. Wachs, D.L. Porter., *Irradiation Performance of U-Mo Alloy Based Monolithic Plate-type Fuel – Design Selection*, INL/EXT-09-16807, Idaho National Laboratory, Idaho, USA, 2009.

30 G. Moore, D. Fox, *RERTR-12 Fabrication Summary Report,* INL/LTD-14-33575, Idaho National Laboratory, Idaho, USA, 2014.

31 G. Moore, *AFIP-6 MK II Fabrication Summary Report,* INL/LTD-12-27302, Idaho National Laboratory, Idaho, USA, 2012.

32 Y. Park, N. Eriksson, D.D. Keiser Jr., J.F. Jue, B. Rabin, G. Moore, Y.H. Sohn., "Microstructural anomalies in hot-isostatic pressed U-10 we.% Mo fuel plates with Zr diffusion barrier," *Mat. Character*, 103 (2015) 50-57.

33 F. Rice, W. Williams, A. Robinson, J. Harp, M. Meyer, B. Rabin, *RERTR-12 Post-irradiation Examination Summary Report,* INL/EXT-14-33066, Idaho National Laboratory, Idaho, USA, 2015

34 W. Williams, F. Rice, A. Robinson, M. Meyer, B. Rabin, *AFIP-6 MKII Post-irradiation Examination Summary Report,* INL/LTD-15-34142, Idaho National Laboratory, Idaho, USA, 2015

35 W.R. Lloyd, J.L. Schulthess, J.K. Wright, B.H. Rabin, R.P. Lind, K.M. Wachs, B.J. Frickey, J. Maupin, *Mechanical Properties Characterization of Irradiated U-10Mo Fuel,* INL/LTD-15-34764, Idaho National Laboratory, Idaho, USA, 2018

36 J.M. Gere, *Mechanics of Materials,* 5th ed., Pacific Grove, CA: Brooks/Cole, 2001

37 J.F. Jue, D. Keiser Jr., C. Breckenridge, B. Rabin, G. Moore, A. Robinson, F. Rice, M. Meyer, *RERTR-12 Characterization Summary Report,* INL/INT-13-29715, Idaho National Laboratory, Idaho, USA, 2013

38 J.F. Jue, C. Breckenridge, T. Trowbridge, T. O'Holleran, D. Keiser Jr., *AFIP-6 MKII Characterization Summary Report,* INL/EXT-14-32457, Idaho National Laboratory, Idaho, USA, 2014

39 W. R. Lloyd, J. Schulthess, K. Wheeler, *AFIP-7 Irradiated U-10Mo Fuel Mechanical Properties Characterization,* ECAR-4051, Idaho National Laboratory, Idaho, USA, 2018.

40 B. Lustman, F. Kerze, *Metallurgy of Zirconium,* McGraw Hill Inc. 1st Edition. New York-Toronto-London (1955)

41 A.M. Garde, R.E. Reed-Hill, “Dual Analysis of Longitudinal and Transverse Zirconium Tensile Stress-strain Data,” ASTM STP-551 (1974) pp. 75-91.

42 C.D. Williams, R.W. Gilbert, “Radiation damage in reactor materials, *Proc. Symp., Vienna, 2-6 June 1969. Vienna: Int. Atomic energy Agency.* Vol. 2, pp 1069.

43 D. Lee, E.F. Koch, “Irradiation damage in Zircaloy-2 produced by high-dose ion bombardment,” *J. Nucl. Mater.*, 50:2 (2974) 162-174.

44 M. Marshall, *RERTR-12 As-Run Neutronics Analysis for Cycles 146A, 146B, 150B, 151A, 151B*, ECAR-3088, Idaho National Laboratory, Idaho, USA, 2016.

45 M.A. Marshall, J.A. Nielsen, *AFIP-6 MkII As-Run Neutronics Analysis for Cycle 151A*, ECAR-3374, Idaho National Laboratory, Idaho, USA, 2016.

46 R. Collette, J. King, D. Keiser, Jr., B. Miller, J. Madden, J. Schulthess, “Fission gas bubble identification using MATLAB’s image processing toolbox,” *Mat. Character,* 118 (2016) 284-293.

47 D.D. Keiser, J.F. Jue, B. Miller, A. Robinson, J. Gan, W. Williams, P. Medvedev, D. Wachs, “SEM and TEM characterization of U-7Mo irradiation to high fission density at relatively high power, high temperature, and high fission rate,” *Proceedings of International Meeting on Reduced Enrichment for Research and Test Reactors (RERTR 2014), Vienna International Center, Vienna, Austria* (2014) (paper S7-P3).

48 M.K. Meyer, J. Gan, J.F. Jue, D.D. Keiser, E. Perez, A. Robinson, D.M. Wachs, N. Woolstenhulme, G.L. Hofman, Y.S. Kim, “Irradiation performance of U-Mo monolithic fuel,” *Nucl. Eng. Technol.,* 46 (2014), pp. 169-182.

49 A. Robinson, *AFIP-6 Baseline Change Report*, INL/LTD-18-50149, Idaho National Laboratory, Idaho, USA, 2018.

50 A. Einstein, “Eine neue Bestimmung der Molekuledimensionen,” *Annalen der Physik,* 19 (1906) 289-306. English translation in “The Collected Papers of Albert Einstein” Vol. 2, Princeton University Press, Sept 1989, accessed online at: https://einsteinpapers.press.princeton.edu/vol2-trans/118

51 Z. Hashin, “The Elastic Moduli of Heterogeneous Materials,” *Journal of Applied Mechanics,* (1962) 143-150

52 M. Eudier, “The mechanical properties of sintered low-alloy steels,” *Powder Metallurgy*, 5 (1962) 278-290.

53 S.K. Hyun, K. Murakami, H. Nakajima, “Anisotropic mechanical properties of porous copper fabricated by unidirectional solidification,” *Materials Science and Engineering,* A299 (2001) 241-248.

54 R.B. Martin, R.R. Haynes, “Confirmation of Theoretical Relation between Stiffness and Porosity in Ceramics,” *J. Am. Concr. Inst.,* 68 (1971) 36-41.

55 R.B. Martin, R.R. Haynes, “Confirmation of Theoretical Relation between Stiffness and Porosity in Ceramics,” *J. Am. Ceram. Soc.*, 54 (1971) 410-411.

56 E.A. Dean, J.A. Lopez, “Empirical Dependence of Elastic Moduli on Porosity for Ceramic Materials,” *J. Am. Ceram. Soc.,* 66 (1983) 366-370.

57 R.E. Fryxell, B.A. Chandler, “Creep, Strength, Expansion, and Elastic Moduli of Sintered BeO as a Function of Grain Size, Porosity, and Grain Orientation,” *J. Am. Ceram. Soc.,* 47 (1964) 283-291.

58 R.W. Rice, “Comparison of stress concentration versus minimum solid area based mechanical property-porosity relations,” *J. Mater. Sci.,* 28 (1993) 2187-2190.

59 R.M. Spriggs, “Expression for Effect of Porosity on Elastic Modulus of Poly-crystalline Refractory Materials, Particularly Aluminum Oxide,” *J. Am. Ceram. Soc.,* 44 (1961) 628-629.

60 R.W. Rice, in “Treatise on Materials Science and Technology” Vol. II (Academic, 1977) p. 199.

61 F.P. Knudson, “Dependence of Mechanical Strength of Brittle Polycrystalline Specimens on Porosity and Grain Size,” *J. Amer. Ceram. Soc.*, 42 (1959) 376.

62 R.W. Rice, S.W. Freiman, “The porosity dependence of fracture energies,” *Ceramic Microstructure,* Bd 76 (1977) 800-812.

63 R.W. Rice, “Pores as fracture origins in ceramics,” *J. Mater. Sci.,* 19 (1984) 895-914.

64 N. Ramakrishnan, V.S. Arunachalam, “Effective elastic moduli of porous solids,” *J. Mater. Sci.,* 25 (1990) 3930-3937.

65 D.P.H. Hasselman, “On the Porosity Dependence of the Elastic Moduli of Poly-crystalline Refactory Materials,” *J. Am. Ceram. Soc.,* 54 (1962) 452-453.

65 Y. Park, N. Eriksson, D.D.Keiser Jr., J.F. Jue, B. Rabin, G. Moore, Y.H. Sohn., “Microstructural anomalies in hot-isostatic pressed U-10 we.% Mo fuel plates with Zr diffusion barrier,” *Mat. Character*, 103 (2015) 50-57.

4 CHAPTER 4: CONCLUSIONS

4.1 Conclusions on un-irradiated U-Mo mechanical properties

Mechanical properties testing using a uniaxial load frame on DU-10Mo foil, cold-rolled to 4 different fabrication conditions was performed to interrogate the influence of fabrication conditions on the properties. Testing was also performed within the range of room temperature to 550°C to evaluate temperature effects on each of the fabrication conditions. From the results we conclude that yield strength is influenced by the different fabrication conditions at the intermediate temperatures tested, with the 50% cold rolled and 20% cold rolled conditions maintaining higher strength at the intermediate temperatures. This result may be the caused by the difference in grain size of these two foil conditions. No evidence of fabrication effect is identified at the highest and lowest test temperatures. From the results, we can also conclude that post-cold-rolling annealing heat treatment on Foil 551-3 produces results (yield stress, ultimate tensile stress) very similar to the hot-rolled only foil (551-5), suggesting this post-cold rolling thermal treatment is effective at substantially recovering tensile properties comparable to hot-rolled only material.

The room-temperature properties appear different from the expected ranges based upon historical data but it is noted that both source-material chemistry and thermo-mechanical processing history of the test specimens can result in significant microstructural differences that may explain these results. Further work is therefore needed to better understand the differences in historical reported properties versus those presented in this work. However, since the exact material chemistry, particularly impurities, and exact fabrication history is not reported in references in the historical work, no direct comparisons can be made.

Both molybdenum banding and carbide impurities creating carbide strings were noted during the characterization. The exact impact of molybdenum banding on mechanical properties, fracture initiation, and crack propagation are not currently known, and may be the subject of future work. The carbide impurities formed into strings in the unannealed foil conditions and demonstrated evidence of crack propagation along this path. Fabrication parameters such as annealing to homogenize the molybdenum banding and the carbide precipitates is recommended to avoid any deleterious effects these characteristics may have on the strength of the bulk material.

4.2 **Conclusions on mechanical properties of irradiated U-Mo alloy**

A suitable methodology and supporting equipment were developed for fabricating, measuring, and testing irradiated fuel specimens in four-point bending. Specimen response data were collected from 36 individual specimens taken from RERTR-12 and AFIP-6 Mk II fuel plates, specimens that exhibited variations in FD from 0.4E+21 to 6.3E+21 f/cm^3, as well as representing various enrichments, unirradiated fuel-foil thicknesses, irradiation conditions, and fuel-plate fabrication processes. Specimen dimensions were measured with calibrated measuring instruments, and the test data were collected using calibrated force and displacement measurements.

Most specimens exhibited essentially elastic behavior up to the point of failure, as expected based on embrittlement of the U-10Mo during irradiation. Basic analysis of the test data from these specimens revealed an expected trend of decreasing bend strength with increasing fission density. Of note, the bend strength of specimens with the lowest fission density (0.4E+21 f/cm^3) were in the 400 MPa range for the bulk specimen and 360 MPa for the U-Mo core, far below the tensile strength of fresh fuel (over 1000 MPa), and showed no signs of any ductility. A trend line for strength, based on all collected test results and analyses, places the bend strength of the U-Mo core at 7E+21 f/cm^3 in the 160 MPa range. There is substantial scatter in the strength data, owing primarily to the brittle nature of the irradiated material, and other potential factors beyond fission density may affect the calculated bend strengths reported.

Four different semi-empirical models of porosity-based modulus degradation were evaluated against the experimental data to determine whether they could accurately describe the experimental data, and the primary cause for degradation being porosity. It was concluded that the non-linear model equation (17) proposed by Ramakrishnan and Arunachalam [64], provided the best fit to the experimental data, but with recommendations that due to uncertainties presented, additional work is needed to further refine the model.

4.3 **Overall Conclusions**

The strength of the irradiated U-Mo as measured by four-point bend testing is significantly reduced when comparted to the strength of the un-irradiated U-Mo evaluated by tensile testing in this work. This occurs even at the lowest burnup evaluated. Beginning of life

irradiation conditions strongly impact the strength of the material. If it is desired to maintain strength of the U-Mo further into the irradiation cycle, additional work must be performed to identify which beginning of life irradiation conditions the material is most sensitive too. For example, is the material most sensitive to accumulated burnup, or perhaps the initial power or temperature. Or is the material sensitive to the initial ramp to power during reactor startup.

The work here reasonably predicted the degradation of the bulk modulus using porosity models, but is limited by the available porosity data. These models are primarily based on principles related to the reduction of solidus area of the material. However, at lower burnup of the U-Mo material, the fission gas is suspended in a superlattice and not yet developed into gross pores. This early life phenomena is not fully accounted for in the existing porosity models and deserves further attention when additional lower burnup porosity data becomes available. Further, the porosity models do not explicitly differentiate between pores filled with fission gas versus pores containing solid fission products. If porosity data becomes available that quantifies the content of fission gas pores, solid fission products, and solidus area the contribution of each to the resultant modulus could be evaluated by a rule of mixtures analysis.

This work is seminal and establishes the baseline mechanical properties of the U-Mo alloy both in the un-irradiated and neutron irradiated state. The U-Mo alloy is being developed to support qualification of a new LEU fuel to support conversions of High Performance Research Reactors. The mechanical properties of the material established here support fuel performance modeling that is necessary to predict the mechanical integrity of the fuel in support of fuel qualification.

4.3.1 Acknowledgements

This manuscript has been authored by Battelle Energy Alliance, LLC under Contract No. DE-AC07-05ID14517 with the U.S. Department of Energy. The U. S. Government retains and the publisher, by accepting the article for publication, acknowledges that the U. S. Government retains a nonexclusive, paid-up, irrevocable, world-wide license to publish or reproduce the published form of this manuscript, or allow others to do so, for U. S. Government purposes. Acknowledgment is given to personnel at the Idaho National Laboratory for their assistance in the accomplishment of this work. Mr. Mike Chappel, Mr. Brian Frickey and Mr. Jake

Maupin made notable contributions to the collection of the experimental data, amongst various other significant contributions from facility and laboratory personal.

4.3.2 Data Availability

The raw/processed data required to reproduce these findings cannot be shared at this time as the data also forms part of an ongoing study.

5 CHAPTER 5: RECOMMENDATIONS

During the performance of this work, several unanswered questions arose, which were outside of the scope of this work to address. One such example is that the impurity content, particularly the carbon impurities can vary from batch to batch of feedstock uranium and can be influenced by the specific thermomechanical processing conditions. More specifically cooling rates during casting can influence how large carbon precipitates become. Both the influence of total carbon content, and the size and distribution of that carbon content were not studied and warrant further investigation of how these variables may impact mechanical properties.

The analysis that was performed on the irradiated U-Mo foil assumed a constant thickness of Zr diffusion barrier. A sensitivity analysis was performed to evaluate the impact of the measured deviation of the Zr thickness on the results, and this was included in the error reporting. However, the Zr thickness is known to vary locally. It is therefore recommended that additional microscopy be performed of samples adjacent to the tested samples, and that more localized values of Zr thickness be used for the analysis.

To reduce fabrication costs, and produce higher yield and more uniform product, there are separate efforts to optimize the thermomechanical rolling process for fabricating the foil. While the work done here included a variety of thermomechanical processing conditions. Changes to the fabrication process should cause future users of this data caution as those process changes can influence the resultant mechanical properties. It is therefore recommended that fabrication process changes be followed up with additional material properties testing.

Appendix A: Publisher Permission to use Authored Content